J. Fluid Mech. (2014), *vol.* 738, *pp.* 591–630.
doi:10.1017/jfm.2013.586

Reactive-infiltration instabilities in rocks. Part 2. Dissolution of a porous matrix

Piotr Szymczak[1],† **and Anthony J. C. Ladd**[2]

[1]Institute of Theoretical Physics, Faculty of Physics, University of Warsaw, Hoża 69, 00-618, Warsaw, Poland

[2]Chemical Engineering Department, University of Florida, Gainesville, FL 32611-6005, USA

(Received 29 March 2013; revised 4 September 2013; accepted 31 October 2013)

A reactive fluid dissolving a uniform porous material triggers an instability in the dissolution front, leading to spontaneous formation of pronounced well-spaced channels in the surrounding rock matrix. The concentration field within the dissolving region contains two different length scales, upstream (no reaction) and downstream of the front position. Previous investigations of the reactive-infiltration instability have considered one or other of the scales to be dominant, leading to rather different conclusions. Here we describe a more general linear stability analysis which includes both length scales simultaneously. We show how previous work corresponds to special cases of our more general analysis and obtain closed-form solutions for small permeability gradients.

Key words: fingering instability, geophysical and geological flows, porous media

1. Introduction

The reactive-infiltration instability (Ortoleva 1994) is a mechanism for pattern development in geology with a range of morphologies and scales, from cave systems running for hundreds of miles (Groves & Howard 1994; Szymczak & Ladd 2011*a*) to laboratory acidization on the scale of centimetres (Daccord & Lenormand 1987). Chemical dissolution is an unusual means of morphological change, in that the patterns are frozen in and can persist for millions of years after the processes leading to them have stopped. Reactive-infiltration instabilities are not limited to groundwater in porous rocks, but occur in magma flows as well (Aharonov *et al.* 1995). Permeable conduits are found in igneous rocks (Spiegelman, Kelemen & Aharonov 2001) and the formation of fingers has been demonstrated experimentally on the centimetre scale (Daines & Kohlstedt 1994).

The reactive-infiltration instability was discovered by petroleum engineers, who noticed that the permeability increase around a wellbore during acidization depended in a non-monotonic way on flow rate (Rowan 1959). The optimum flow rate, producing the largest increase in permeability for a given amount of acid, was found to correspond to the spontaneous development of highly localized flow paths, which they have called ‘wormholes’. Wormholes are the end result of a positive feedback

† Email address for correspondence: piotrek@fuw.edu.pl

between spatial variations in porosity in the initial matrix and the local dissolution rate. A small enhancement in porosity at some point in the reaction front increases the fluid flow in that region, which convects reactant further downstream. By this means any local variation in porosity is amplified as the reaction front passes through and propagates downstream with the front, eventually developing into wormholes.

Theories of the reactive-infiltration instability have proceeded from two different standpoints: those with an emphasis on natural processes taking place over thousands (or millions) of years have started from a limiting case where diffusion dominates (Chadam *et al.* 1986; Ortoleva *et al.* 1987*a*), whereas work derived from interest in petroleum recovery has focused on much more rapid flows assuming diffusion to be negligible (Sherwood 1987; Hinch & Bhatt 1990). In fact there are in general two length scales characterizing the reactant concentration in a steadily propagating front; an upstream length where the material is fully dissolved and a downstream length over which it transitions to the undissolved state. The apparently disparate theories of the reactive-infiltration instability are limiting cases where one or the other of the two length scales vanishes in comparison with the other (Szymczak & Ladd 2013).

Here we present a comprehensive analysis of the stability of a planar reaction front in a homogeneous porous matrix, spanning the complete range of reaction rates and flow rates. In §§ 2 and 3 we develop a general theory for the linear instability and in subsequent sections we consider three limiting cases: a small porosity contrast (§ 4) where we can neglect changes in dispersion and specific surface area on either side of the front, the thin-front limit (§ 5) where the interface is treated as a discontinuity in porosity and the convective limit (§ 6) where dispersion is negligible. Closed-form solutions are obtained when the permeability gradient is small. This paper complements a recent stability analysis of fracture dissolution (Szymczak & Ladd 2012).

There is a related body of work on chemohydrodynamic instabilities, usually involving the interplay of diffusion, convection and reaction; examples include miscible chromatographic separations, fixed bed chemical processing and regeneration, frontal polymerization, viscous fingering of reactive fluids and chemical treatment of oil-bearing formations (De Wit & Homsy 1999; De Wit, Eckert & Kalliadasis 2012). In most of these systems a coupling between fluid mobility and concentration drives the instability. For example, in miscible displacements (Homsy 1987; De Wit & Homsy 1999) the mobility contrast comes about from the concentration dependence of viscosity, which leads to the appearance of fingering patterns not unlike those observed in dissolution problems. However, in reactive-infiltration systems the mobility contrast is caused by dissolution of matrix material, and is therefore irreversible (De Wit & Homsy 1999). In most of the other chemohydrodynamic systems, a given flow region can eventually recover its original mobility, which may lead to a more complex morphology than in reactive infiltration.

2. Governing equations

When a porous matrix is infiltrated by an incoming flux of reactive fluid, a front develops once all of the soluble material at the inlet has been dissolved. This front propagates into the matrix as illustrated in figure 1, which shows the position of the front (solid line) some time later. Upstream of the front, all of the soluble material has dissolved and the porosity is constant, $\phi = \phi_1$. Ahead of the front the porosity decays gradually to its value in the undisturbed matrix, $\phi = \phi_0$. The front is initially planar

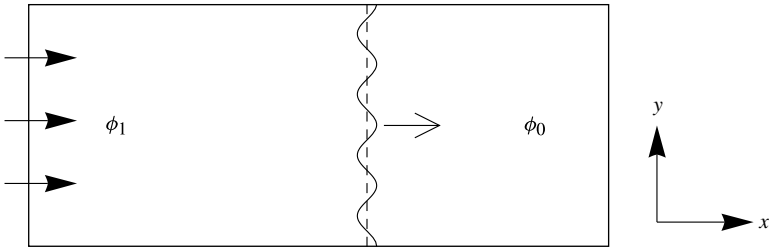

FIGURE 1. Geometry of the reactive-infiltration instability. A constant flux of reactive fluid is injected from the left face and dissolves the porous matrix through chemical reactions at the solid surface. Once dissolution at the inlet is complete, the reaction front, shown by the solid line, advances into the matrix. The mean front position after some time t is indicated by the dashed line.

but eventually breaks up because of a positive feedback between flow and dissolution, which amplifies any small variation in the porosity field (Chadam *et al.* 1986).

On scales large compared with the pore size, the velocity of the fluid is proportional to the pressure gradient (Darcy's law),

$$\boldsymbol{v} = -K\frac{\boldsymbol{\nabla} p}{\mu}, \tag{2.1}$$

where $\boldsymbol{v}$ is the Darcy velocity, ϕ is the porosity and $K(\phi)$ is the permeability, which we will assume to be isotropic. When there is dissolution, the velocity field is no longer divergence free and the continuity equation is

$$\partial_t \phi + \boldsymbol{\nabla}\cdot\boldsymbol{v} = 0. \tag{2.2}$$

The transport of reactants and products is described by a convection–diffusion–reaction equation,

$$\partial_t(\phi c) + \boldsymbol{\nabla}\cdot(\boldsymbol{v}c) - \boldsymbol{\nabla}\cdot(\boldsymbol{D}\cdot\boldsymbol{\nabla} c) = -R, \tag{2.3}$$

where $\boldsymbol{D}$ is the dispersion tensor. We use a constitutive law suitable for an isotropic material (Bear 1961; Golfier *et al.* 2002):

$$\boldsymbol{D}(\phi, \boldsymbol{v}) = \left(D^E + \Theta^T|\boldsymbol{v}|\right)\mathbf{1} + \left(\Theta^L - \Theta^T\right)\frac{\boldsymbol{v}\boldsymbol{v}}{|\boldsymbol{v}|}, \tag{2.4}$$

where $D^E(\phi)$, $\Theta^L(\phi)$ and $\Theta^T(\phi)$ are functions of porosity only. If the porosity is large enough, these coefficients are simply proportional to ϕ. In typical geophysical flows, where the pore-scale Péclet number is small, $\boldsymbol{D} \to D^E\mathbf{1}$, where D^E is the effective diffusion coefficient of the reactant in the porous matrix. However, in laboratory experiments or reservoir acidization, the flow velocities can be much larger and hydrodynamic dispersion, proportional to Θ^L and Θ^T, becomes important.

For simplicity we will assume a linear kinetic equation for the reaction rate,

$$R(c) = ksc, \tag{2.5}$$

where k is the rate constant and s is the reactive surface area per unit volume; the effects of higher-order rate laws on the instability growth rate can be largely subsumed into the reaction length scale $l_p \sim v(\mathrm{d}R/\mathrm{d}c)^{-1}$ (Szymczak & Ladd 2012).

Equation (2.5) assumes that the rate constant and characteristic pore size are sufficiently small that diffusion within the pore spaces is fast in comparison with

the reactive flux, $k/Ds \ll 1$. Typical specific surface areas in rocks are in the range 10^3–10^5 cm^{-1} and under geophysical conditions the dissolution kinetics of porous rocks are usually reaction limited. Possible exceptions include the dissolution of calcite by a strong acid and the dissolution of gypsum by aqueous CO_2, where reaction rates can be as high as 0.1 cm s^{-1}. Furthermore, as wormholes develop, diffusion of reactant across the empty space within the wormhole will most likely become the rate-limiting process, but during the initial breakup of the front it is reasonable to assume the kinetics are reaction limited. Details of the averaging methods that can be used to derive (2.1)–(2.5) from the underlying pore-scale processes are given in appendix A of Golfier *et al.* (2002).

Dissolution of the matrix by the reactive fluid gives rise to a time-dependent porosity field,

$$\nu c_{sol} \partial_t \phi = ksc, \tag{2.6}$$

where c_{sol} is the concentration of the solid species and ν accounts for the stoichiometry of the reaction. The acid capacity number $\gamma_a = c_{in}/\nu c_{sol}(\phi_1 - \phi_0)$ is defined as the volume of rock (molar concentration c_{sol}) that is completely dissolved by a unit volume of reactant (molar concentration c_{in}). In typical geophysical systems the reactant is dilute ($c_{in} \ll c_{sol}$) and therefore $\gamma_a \ll 1$; for example, when calcite is dissolved by aqueous CO_2, $\gamma_a \sim 10^{-4}$. Whenever $\gamma_a \ll 1$ the velocity and concentration fields will reach steady state well before any significant change in porosity. We can therefore assume that the continuity (2.2) and transport (2.3) equations are stationary (Szymczak & Ladd 2012):

$$v_x \partial_x c + v_y \partial_y c - (\nabla \cdot \boldsymbol{D} \cdot \nabla c) = -ksc \quad \text{(transport)} \tag{2.7}$$

$$\partial_t \phi = ks\gamma_a(\phi_1 - \phi_0)\frac{c}{c_{in}} \quad \text{(erosion)} \tag{2.8}$$

$$\partial_x v_x + \partial_y v_y = 0 \quad \text{(continuity)} \tag{2.9}$$

$$\partial_y v_x - v_x W \partial_y \phi = \partial_x v_y - v_y W \partial_x \phi \quad \text{(compatibility)} \tag{2.10}$$

The compatibility equation (2.10) follows from (2.1), eliminating the pressure by cross-differentiation $\partial_y \left(K^{-1} v_x\right) = \partial_x \left(K^{-1} v_y\right)$, with

$$W(\phi) = \frac{\mathrm{d} \ln K}{\mathrm{d}\phi}. \tag{2.11}$$

Solutions of these equations depend on the constitutive laws for the permeability $K(\phi)$, specific surface area, $s(\phi)$, and the coefficients in the dispersion tensor $\boldsymbol{D}(\phi, \boldsymbol{v})$ (equation (2.4)).

The stability analysis assumes that the solutions are periodic in the plane transverse to the flow (yz) and (2.7)–(2.10) will therefore be closed by boundary conditions on the velocity and concentration fields as $x \to \pm\infty$, together with an initial condition on the porosity:

$$\boldsymbol{v}(x \to -\infty) = v_0 \boldsymbol{e}_x, \quad v_y(x \to \infty) = 0, \tag{2.12}$$

$$c(x \to -\infty) = c_{in}, \quad (\partial_x c)_{x\to\infty} = 0, \tag{2.13}$$

$$\phi(t \to -\infty) = \phi_0. \tag{2.14}$$

The initial condition on ϕ must be applied in the distant past to allow time for the front to develop.

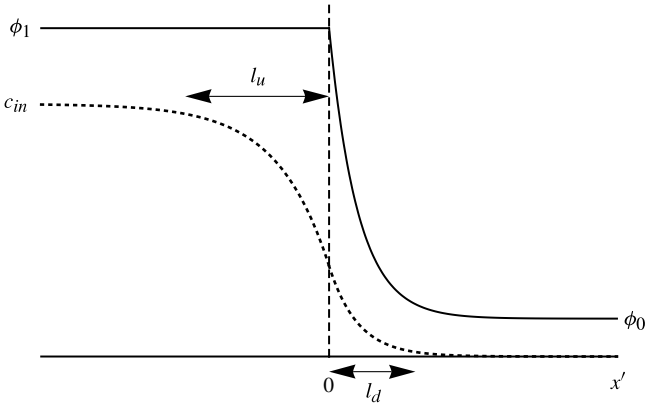

FIGURE 2. Concentration and porosity profiles in the moving front frame $x' = x - Ut$; the position of the front is indicated by the dashed vertical line. The concentration profile decays with different length scales, l_u and l_d, in the upstream ($x' < 0$) and downstream ($x' > 0$) regions.

2.1. *One-dimensional solutions*

Equations (2.7)–(2.10) have stationary one-dimensional solutions for the porosity $\phi_b(x')$ and concentration $c_b(x')$ in a frame moving with the velocity of the dissolution front, U:

$$v_0 \partial_{x'} c_b - \partial_{x'} D_b^L \partial_{x'} c_b = -k s_b c_b, \tag{2.15}$$

$$-U \partial_{x'} \phi_b = k s_b \gamma_a (\phi_1 - \phi_0) \frac{c_b}{c_{in}}, \tag{2.16}$$

where v_0 is the (constant) velocity of the fluid in the matrix. The moving frame, $x' = x - Ut$, has its origin at the front position, as indicated in figure 2. The velocity of the front is determined by a mass balance on the reactant, $v_0 c_{in} = U\nu(\phi_1 - \phi_0)c_{sol}$;

$$U = \gamma_a v_0. \tag{2.17}$$

These one-dimensional fields form the base solutions for the linear stability analysis.

The dispersion tensor in the base state $\boldsymbol{D}_b$ is diagonal,

$$\boldsymbol{D}_b = \begin{pmatrix} D_b^L & 0 \\ 0 & D_b^T \end{pmatrix} = \begin{pmatrix} D_b^E + \Theta_b^L v_0 & 0 \\ 0 & D_b^E + \Theta_b^T v_0 \end{pmatrix}, \tag{2.18}$$

because the flow is uniaxial. For small deviations from the one-dimensional state (2.15), only the functions D_b^E, D_b^L and D_b^T are needed to characterize dispersion, as shown in (A 9) and (A 10); note that the dispersion coefficients $D_b^{L,T}$ depend parametrically on the base-state fluid velocity as well as the porosity.

Steady reactive infiltration, as described by (2.15)–(2.17), is illustrated in figure 2. Reactant is injected upstream with a concentration c_{in} and is consumed in the region downstream of the front ($x' > 0$); upstream of the front all of the soluble material has dissolved and the reaction term vanishes. However, because of the diffusive flux of depleted reactant, the concentration upstream of the front decays (from c_{in}), with a

penetration length

$$l_u = \frac{D_1^L}{v_0}, \tag{2.19}$$

where $D_1^L = D_b^L(\phi_1)$. Downstream from the front the porosity decays to its value in the undisturbed matrix, ϕ_0; the specific surface area and dispersion are then constant: $s_b(\phi_0) = s_0$ and $D_b^L(\phi_0) = D_0^L$. The concentration has a natural length scale far downstream, l_d, which follows from the solution of (2.15) (with porosity-independent coefficients),

$$l_d = \frac{2D_0^L}{\sqrt{v_0^2 + 4ks_0D_0^L} - v_0}. \tag{2.20}$$

The distinct length scales make the problem more complicated to analyse, but also more rich than has been generally suspected. Scaling length by l_d, $\xi = x'/l_d$, introduces two dimensionless parameters into the concentration equation far downstream ($\xi \to \infty$),

$$\partial_\xi c_b - Pe^{-1}\partial_\xi^2 c_b = -Da\, c_b, \tag{2.21}$$

which can be identified as Péclet and Damköhler numbers on the penetration length scale l_d: (Szymczak & Ladd 2012),

$$Pe = \frac{v_0 l_d}{D_0^L}, \quad Da = \frac{ks_0 l_d}{v_0}. \tag{2.22}$$

Péclet and Damköhler numbers are usually defined by the pore size or the sample size, but since geophysical systems are typically unbounded, the reactant penetration length is the largest and therefore the most important length scale. Interestingly, Pe and Da are not independent, but $Da = 1 + Pe^{-1}$. In essence the choice of length scale means that the reaction term is never negligible, $Da > 1$.

On the scale of the penetration length l_d, the transition between convective and dispersive limits is controlled by the reaction rate as well as the fluid velocity, through the parameter

$$H = \frac{D_0^L ks_0}{v_0^2} = \frac{Da}{Pe}, \tag{2.23}$$

which appears in l_d (2.20). The Péclet and Damköhler numbers are related to H:

$$Pe = \frac{2}{\sqrt{1+4H} - 1}, \quad Da = \frac{2H}{\sqrt{1+4H} - 1}; \tag{2.24}$$

thus, on the scale of l_d there is a single parameter (H) which characterizes the relative contributions of convection, dispersion and reaction. Small H corresponds to convection-dominated dissolution ($l_d \gg l_u$), whereas large H means dispersion dominates ($l_u \gg l_d$). The reaction rate enters into the competition between convection and dispersion by changing the scale over which the front develops (Lichtner 1988; Phillips 1990). When the reaction is slow the width of the front is large ($l_d \to v_0/ks_0$) making convection more important, but when the reaction is fast ($l_d \to \sqrt{D_0^L/ks_0}$) dispersion tends to be dominant.

2.2. *Scaling*

The dissolution equations (2.7)–(2.10) can be simplified by transforming to dimensionless variables, using either l_u or l_d to scale distance. In general, we will use the downstream length l_d, although in the diffusive limit studied by Chadam *et al.* (1986) and Ortoleva *et al.* (1987*a*) the upstream length must be used because l_d vanishes; there is no single scaling that includes both convective and diffusive limits. Taking the downstream penetration length l_d as the characteristic length and $t_d = l_d/v_0\gamma_a$ as the characteristic time scale we define dimensionless coordinates and time as

$$\xi = \frac{x'}{l_d}, \quad \eta = \frac{y}{l_d}, \quad \tau = \frac{t}{t_d} = \frac{\gamma_a v_0 t}{l_d}. \tag{2.25}$$

The choice of time scale differs from our previous work (Szymczak & Ladd 2011*b*, 2012) but reduces to the same scaling in the convective limit, where the penetration length is simply v_0/ks_0. The new scaling has the advantage that the dimensionless front velocity $\hat{U} = Ut_d/l_d = 1$ (2.17), which means that the dimensionless operators for space (∂_ξ) and time (∂_τ) are on the same scale.

Dimensionless fields, porosity, concentration and velocity, can be defined as

$$\hat{\phi} = \frac{\phi - \phi_0}{\phi_1 - \phi_0}, \quad \hat{c} = \frac{c}{c_{in}}, \quad \hat{\boldsymbol{v}} = \frac{\boldsymbol{v}}{v_0}, \tag{2.26}$$

together with a corresponding scaling for the permeability, specific surface area and dispersion,

$$\hat{W} = \frac{d\ln(K/K_0)}{\mathrm{d}\hat{\phi}}, \quad \hat{s} = \frac{s}{s_0}, \quad \hat{\boldsymbol{D}} = \frac{\boldsymbol{D}}{v_0 l_d}. \tag{2.27}$$

The parameters Pe and Da (2.22) are related to the dimensionless longitudinal dispersion coefficient in the unaltered matrix, $\hat{D}_0^L = D_0^L/v_0 l_d$:

$$Pe^{-1} = \hat{D}_0^L, \quad Da = 1 + \hat{D}_0^L. \tag{2.28}$$

The downstream equations in the moving-front frame are, from (2.7)–(2.10),

$$\hat{v}_\xi \partial_\xi \hat{c} + \hat{v}_\eta \partial_\eta \hat{c} - \hat{\boldsymbol{\nabla}} \cdot \hat{\boldsymbol{D}} \cdot \hat{\boldsymbol{\nabla}} \hat{c} = -(1 + \hat{D}_0^L)\hat{s}\hat{c}, \tag{2.29}$$

$$\partial_\tau \hat{\phi} - \partial_\xi \hat{\phi} = (1 + \hat{D}_0^L)\hat{s}\hat{c}, \tag{2.30}$$

$$\partial_\xi \hat{v}_\xi + \partial_\eta \hat{v}_\eta = 0, \tag{2.31}$$

$$\partial_\eta \hat{v}_\xi - \hat{v}_\xi \hat{W} \partial_\eta \hat{\phi} = \partial_\xi \hat{v}_\eta - \hat{v}_\eta \hat{W} \partial_\xi \hat{\phi}, \tag{2.32}$$

where $\hat{\boldsymbol{\nabla}} \equiv [\partial_\xi, \partial_\eta]$. Upstream of the front, which we indicate by the superscript u, there is no reaction and the porosity is therefore constant, $\hat{\phi} = 1$:

$$\hat{v}_\xi^u \partial_\xi \hat{c}^u + \hat{v}_\eta^u \partial_\eta \hat{c}^u - \hat{\boldsymbol{\nabla}} \cdot \hat{\boldsymbol{D}}_1 \cdot \hat{\boldsymbol{\nabla}} \hat{c}^u = 0, \tag{2.33}$$

$$\partial_\xi^2 \hat{v}_\xi^u + \partial_\eta^2 \hat{v}_\xi^u = 0, \tag{2.34}$$

where $\hat{\boldsymbol{D}}_1$ indicates the dispersion tensor in the fully dissolved matrix. In (2.34), v_η was eliminated through the incompressibility condition (2.31).

2.3. *Notation*

For future reference, here we summarize the notation we have introduced. The most common symbols in the paper are listed in table 1. In addition we employ the

ϕ	Downstream porosity	$\boldsymbol{v}$	Downstream velocity	c	Downstream concentration
ϕ_1	Upstream porosity	$\boldsymbol{v}^u$	Upstream velocity	c^u	Upstream concentration
K	Permeability	s	Specific surface area	k	Rate constant
Δ	Porosity contrast (4.1)	Γ	Permeability contrast (5.2)	W	Permeability gradient (2.11)
D^E	Diffusion (2.4)	D^L	Longitudinal dispersion	D^T	Transverse dispersion
c_{in}	Inlet concentration	γ_a	Acid capacity (2.6)		
U	Front velocity (2.17)	l_u	Upstream length (2.19)	l_d	Downstream length (2.20)
H	(2.23)	Pe	(2.22)	Da	(2.22)
ξ, η, τ	Scaled coordinates (2.25)	u	Wavenumber (3.1)	ω	Growth rate (3.1)
ξ_f	Front position (3.24)	λ_c	(3.26)	Λ	(3.27)

TABLE 1. Notation: the key symbols are listed and equations referenced where appropriate.

subscript b to indicate a base solution for the linear stability analysis; either a steady one-dimensional field (e.g. ϕ_b, c_b) or a quantity derived from one-dimensional fields, e.g. $\boldsymbol{D}_b$ (equation (2.18)). The superscript u denotes an upstream field, while the subscripts 0 and 1 are used to denote fields in the undisturbed and fully dissolved matrix, respectively. In § 4, where the distinction between upstream and downstream properties vanishes, the subscripts will be omitted; in addition, when dispersion can be replaced by isotropic diffusion (e.g. §§ 4.1.2 and 5.1), the coefficients D^L, D^T, D^E will be replaced a single diffusivity, D. A superscript prime denotes differentiation with respect to porosity, e.g. (3.11); it is only used for dimensionless quantities. Finally, non-dimensional fields are indicated with a caret, for example $\hat{\phi}$. In general, fields are made dimensionless by scaling with their value in the undisturbed matrix; for example $\hat{s} = s/s_0$ (equation (2.27)). Exceptions are $\hat{c} = c/c_{in}$, which is scaled by the inlet concentration, and $\hat{\phi}$ which is shifted by ϕ_0 and scaled by $\phi_1 - \phi_0$ (equation (2.26)); in both cases the dimensionless fields are bounded by [0, 1]. There is a second scaling of the wavenumber and growth rate, based on the upstream length scale (4.14), which is introduced in § 4.1 to describe the regime where the downstream penetration length vanishes; we use a tilde to indicate this alternative scaling.

3. Linear stability analysis

The planar reaction fronts suggested by (2.15) and (2.16) are unstable to infinitesimal perturbations about the base one-dimensional solution (Chadam *et al.* 1986; Ortoleva *et al.* 1987*a*; Sherwood 1987; Hinch & Bhatt 1990; Kelemen *et al.* 1995; Szymczak & Ladd 2011*a*). We use linear stability analysis to determine the growth rate ω of perturbations with wavelength λ:

$$\hat{\phi} = \hat{\phi}_b + f_\phi(\xi)\cos(\hat{u}\eta)\mathrm{e}^{\hat{\omega}\tau} \tag{3.1}$$

$$\hat{c} = \hat{c}_b + f_c(\xi)\cos(\hat{u}\eta)\mathrm{e}^{\hat{\omega}\tau}, \tag{3.2}$$

$$\hat{v}_\xi = 1 + f_v(\xi)\cos(\hat{u}\eta)\mathrm{e}^{\hat{\omega}\tau}, \tag{3.3}$$

$$\hat{u}\hat{v}_\eta = -\partial_\xi f_v(\xi)\sin(\hat{u}\eta)\mathrm{e}^{\hat{\omega}\tau}, \tag{3.4}$$

where $\hat{u} = 2\pi l_d/\lambda$ and $\hat{\omega} = \omega t_d$. The incompressibility condition (2.31) was used to eliminate the independent variation in $\hat{v}_\eta$ and reduce the number of unknown fields to three. The linear stability analysis then reduces to solving three coupled ordinary

differential equations (appendix A),

$$\begin{pmatrix} \mathscr{L}_{vv} & \mathscr{L}_{vc} & \mathscr{L}_{v\phi} \\ 0 & -(1+\hat{D}_0^L)\hat{s}_b & \mathscr{L}_{c\phi} \\ \mathscr{L}_{\phi v} & 0 & \hat{W}_b\hat{u}^2 \end{pmatrix} \begin{pmatrix} f_v \\ f_c \\ f_\phi \end{pmatrix} = \mathbf{0}, \tag{3.5}$$

where the linear operators depend only on the base state porosity and concentration:

$$\mathscr{L}_{vv} = (\partial_\xi \hat{c}_b) - \left[\partial_\xi(\hat{D}_b^L - \hat{D}_b^E)(\partial_\xi \hat{c}_b) - (\hat{D}_b^L - \hat{D}_b^T)(\partial_\xi \hat{c}_b)\partial_\xi\right], \tag{3.6}$$

$$\mathscr{L}_{vc} = \partial_\xi - \left[\partial_\xi \hat{D}_b^L \partial_\xi - \hat{D}_b^T \hat{u}^2\right], \tag{3.7}$$

$$\mathscr{L}_{v\phi} = \hat{\omega} - \partial_\xi - \partial_\xi(\hat{D}_b^L)'(\partial_\xi \hat{c}_b), \tag{3.8}$$

$$\mathscr{L}_{c\phi} = \hat{\omega} - \partial_\xi - (1+\hat{D}_0^L)\hat{s}_b' \hat{c}_b, \tag{3.9}$$

$$\mathscr{L}_{\phi v} = \partial_\xi^2 - \hat{u}^2 - \hat{W}_b(\partial_\xi \hat{\phi}_b)\partial_\xi. \tag{3.10}$$

The prime indicates a derivative with respect to porosity, e.g.

$$\hat{s}_b' = \left(\frac{\mathrm{d}\hat{s}}{\mathrm{d}\hat{\phi}}\right)_{\hat{\phi}_b}, \tag{3.11}$$

and partial derivatives in parentheses only operate on functions within the same pair of parentheses.

The equations for the region upstream of the front can be obtained in a similar fashion:

$$\begin{pmatrix} \mathscr{L}_{vv}^u & \mathscr{L}_{vc}^u \\ \mathscr{L}_{\phi v}^u & 0 \end{pmatrix} \begin{pmatrix} f_v^u \\ f_c^u \end{pmatrix} = \mathbf{0}, \tag{3.12}$$

$$\mathscr{L}_{vv}^u = (\partial_\xi \hat{c}_b^u) - \left[(\hat{D}_1^T - \hat{D}_1^E)(\partial_\xi \hat{c}_b^u)\partial_\xi + (\hat{D}_1^L - \hat{D}_1^E)(\partial_\xi^2 \hat{c}_b^u)\right], \tag{3.13}$$

$$\mathscr{L}_{vc}^u = \partial_\xi - \left[\hat{D}_1^L \partial_\xi^2 - \hat{D}_1^T \hat{u}^2\right], \tag{3.14}$$

$$\mathscr{L}_{\phi v}^u = \partial_\xi^2 - \hat{u}^2. \tag{3.15}$$

The coefficients $\hat{\boldsymbol{D}}_1 = \hat{\boldsymbol{D}}_b(\hat{\phi} = 1)$ are constants, calculated at the porosity of the fully dissolved matrix.

3.1. *Boundary conditions*

The base solutions and perturbations are determined separately in the regions upstream and downstream of the front. The solutions must be matched at the front, which gives the following boundary conditions and continuity conditions:

$$\hat{v}_\xi^u(-\infty) = 1, \quad \hat{v}_\xi^u(\xi_f) = \hat{v}_\xi(\xi_f), \quad (\partial_\xi \hat{v}_\xi^u)_{\xi_f} = (\partial_\xi \hat{v}_\xi)_{\xi_f}, \quad (\partial_\xi \hat{v}_\xi)_\infty = 0; \tag{3.16}$$

$$\hat{c}^u(-\infty) = 1, \quad \hat{c}^u(\xi_f) = \hat{c}(\xi_f), \quad (\partial_\xi \hat{c}^u)_{\xi_f} = (\partial_\xi \hat{c})_{\xi_f}, \quad (\partial_\xi \hat{c})_\infty = 0; \tag{3.17}$$

$$1 = \hat{\phi}(\xi_f), \quad \hat{\phi}(\infty) = 0. \tag{3.18}$$

Both concentration and its derivative must be matched at the front in order to ensure continuity of the reactant flux (convective and diffusive). The conditions on $\partial_\xi \hat{v}_\xi$ in (3.16) follow from the continuity of the tangential velocity across the front and

the divergence-free velocity field (2.9). The initial condition on the porosity field, $\hat{\phi}(t \to -\infty) = 0$, translates into the downstream boundary condition in the moving front frame $\hat{\phi}(\infty) = 0$. The condition at the front, $\hat{\phi}(\xi_f) = 1$, follows from the additional requirement that the front velocity remains constant, $\mathrm{d}x_f/\mathrm{d}t = U$, so that the front remains stationary in the comoving frame. It is always possible to determine the solution upstream of the front in closed form because of the constant porosity field and absence of dissolution; this also forms the basis for the analysis of the thin-front limit (Chadam *et al.* 1986). We will use the upstream fields to obtain boundary conditions on the downstream base solutions and perturbations (3.5).

3.1.1. *Base solutions*

The dimensionless base solutions depend on the constitutive models for $\hat{D}_b^L$ and $\hat{s}_b$:

$$\partial_\xi \hat{c}_b - \partial_\xi \hat{D}_b^L \partial_\xi \hat{c}_b = -(1 + \hat{D}_0^L)\hat{c}_b \hat{s}_b, \tag{3.19}$$

$$\partial_\xi \hat{\phi}_b = -(1 + \hat{D}_0^L)\hat{c}_b \hat{s}_b; \tag{3.20}$$

once again the Damköhler number in the scaling of (2.22) is $Da = 1 + \hat{D}_0^L$ (2.28). There are no explicit solutions in the general case, but as $\xi \to \infty$ ($\hat{D}_b^L \to \hat{D}_0^L$ and $\hat{s}_b \to 1$), they decay exponentially

$$\hat{\phi}_b \sim \mathrm{e}^{-\xi}, \quad \hat{v}_{b,\xi} = 1, \quad \hat{c}_b \sim \mathrm{e}^{-\xi}. \tag{3.21}$$

Upstream of the front, where all of the soluble material has dissolved, the base solutions are

$$\hat{\phi}_b^u = 1, \quad \hat{v}_{b,\xi}^u = 1, \quad \hat{c}_b^u = 1 - B\mathrm{e}^{\xi/\hat{D}_1^L}, \tag{3.22}$$

where B is a constant. The matching conditions on the porosity and concentration fields result in the following boundary conditions on the downstream base fields:

$$\hat{\phi}_b(0) = 1, \quad \hat{D}_1^L(\partial_\xi \hat{c}_b)_0 - \hat{c}_b(0) + 1 = 0. \tag{3.23}$$

In deriving the concentration boundary condition, the upstream base solution (3.22) was used to relate the derivative of $\hat{c}_b$ at the front to $\hat{c}_b$ itself (3.17).

3.1.2. *Perturbations*

The upstream perturbations can be found explicitly, even in the most general case, because the porosity is constant. Here we use these solutions to derive boundary conditions on the downstream solutions. Perturbations in the front (relative to its mean position) are assumed to grow exponentially in time, as with the other fields,

$$\xi_f(\eta, \tau) = \xi_0 \cos(\hat{u}\eta)\mathrm{e}^{\hat{\omega}\tau}, \tag{3.24}$$

with an initial amplitude ξ_0. Boundary conditions must be evaluated along the front itself, and then converted to the mean position ($\xi = 0$) by linearization.

Upstream of the front f_v^u satisfies the Laplace equation, and acts as a forcing term in the equation for f_c^u. The dispersion coefficients in (3.13)–(3.14) are constant, and solutions of (3.12) satisfying the far-field boundary conditions contain a total of two unknown coefficients to be matched to the downstream solutions:

$$f_v^u = A_v \mathrm{e}^{\hat{u}\xi} \quad f_c^u = A_c \mathrm{e}^{\lambda_c \xi} - A_v (\mathscr{L}_{vc}^u)^{-1} \mathscr{L}_{vv}^u \mathrm{e}^{\hat{u}\xi}, \quad f_\phi^u = 0, \tag{3.25}$$

where λ_c is the positive eigenvalue of $\mathscr{L}^u_{vc}$,

$$\lambda_c = \frac{1 + \sqrt{1 + 4\hat{D}_1^L \hat{D}_1^T \hat{u}^2}}{2\hat{D}_1^L}. \tag{3.26}$$

The function $(\mathscr{L}^u_{vc})^{-1}\mathscr{L}^u_{vv} e^{\hat{u}\xi} = \Lambda(\xi)$ has the explicit form

$$\Lambda(\xi) = \frac{(-\partial_\xi \hat{c}_b)_0 \left[\hat{D}_1^E/\hat{D}_1^L - \hat{u}(\hat{D}_1^T - \hat{D}_1^E)\right]}{\hat{u}\left[1 + \hat{u}(\hat{D}_1^L - \hat{D}_1^T)\right]} e^{(\hat{u}+1/\hat{D}_1^L)\xi}, \tag{3.27}$$

where we have made use of the result $(\partial_\xi \hat{c}^u_b) = (\partial_\xi \hat{c}^u_b)_0 \, e^{\xi/\hat{D}_1^L}$ from (3.22).

The five matching conditions at the front in (3.16)–(3.18) are used to eliminate the unknown coefficients in the upstream solutions and obtain three additional boundary conditions, which then close the downstream equations and determine the eigenvalue $\hat{\omega}(\hat{u})$. The downstream porosity at the front $\hat{\phi}(\xi_f)$ can be written to linear order in the perturbations, ξ_f and $\delta\hat{\phi} = \hat{\phi} - \hat{\phi}_b$, as

$$\hat{\phi}(\xi_f) = \hat{\phi}_b(0) + \xi_f(\partial_\xi \hat{\phi}_b)_0 + \delta\hat{\phi}(0), \tag{3.28}$$

with $\hat{\phi}(\xi_f) = 1 = \hat{\phi}_b(0)$. The boundary condition on the downstream perturbation f_ϕ at the mean front position ($\xi = 0$) is then

$$f_\phi(0) = \xi_0(-\partial_\xi \hat{\phi}_b)_0. \tag{3.29}$$

Continuity of velocity can be established at the mean front position directly, because the base velocity field is constant. Using the matching conditions in (3.16):

$$A_v = f_v(0), \quad \hat{u}A_v = (\partial_\xi f_v)_0, \tag{3.30}$$

which gives the boundary condition on the downstream velocity perturbation

$$(\partial_\xi f_v)_0 - \hat{u} f_v(0) = 0. \tag{3.31}$$

The boundary condition for the downstream concentration perturbation can be derived by linearizing the matching conditions in (3.17) as in (3.28):

$$f_c(0) = f_c^u(0), \tag{3.32}$$

$$(\partial_\xi f_c)_0 = (\partial_\xi f_c^u)_0 - \xi_0 \left[(\partial_\xi^2 \hat{c}_b)_0 - (\partial_\xi^2 \hat{c}^u_b)_0\right]. \tag{3.33}$$

From (3.25), the right-hand side of (3.33) contains two constants: $A_v = f_v(0)$ (equation (3.30)) and $A_c = f_c(0) + f_v(0)\Lambda(0)$ (equation (3.25)), where $\Lambda(\xi)$ is given in (3.27). There is an additional constant from the base solution (3.22) in $(\partial_\xi^2 \hat{c}^u_b)_0$, but this can be related to the downstream concentration near the front, $(\partial_\xi^2 \hat{c}^u_b)_0 = (\partial_\xi \hat{c}^u_b)_0/\hat{D}_1^L = (\partial_\xi \hat{c}_b)_0/\hat{D}_1^L$.

Eliminating A_c and A_v from the upstream perturbations given in (3.25) gives the boundary condition on f_c in terms of the downstream fields only,

$$(\partial_\xi f_c)_0 = \lambda_c f_c(0) + \left[\lambda_c - \frac{1}{\hat{D}_1^L} - \hat{u}\right]\Lambda(0) f_v(0) - \xi_0 \left[(\partial_\xi^2 \hat{c}_b)_0 - \frac{1}{\hat{D}_1^L}(\partial_\xi \hat{c}_b)_0\right]. \tag{3.34}$$

The amplitude ξ_0 multiplies f_v and f_c as well as f_ϕ (equation (3.29)), and therefore drops out of the final equation for the growth rate.

3.2. *Summary*

The key results of our analysis are contained in the equations for the downstream perturbations (3.5), together with the boundary conditions (3.29), (3.31) and (3.34). The upstream problem has been entirely subsumed into the boundary conditions on the downstream solution. Constitutive laws for dispersion and specific surface area usually preclude an analytic solution for the base profiles, but we will limit the detailed analysis to cases where an explicit form for the base profiles can be found. The equations for the perturbations are usually solved numerically, but in some cases an analytic solution of the dispersion relation can be obtained (§§ 4.1 and 5).

4. Small porosity contrast: $\phi_1 \to \phi_0$

A number of rock formations are composed of small amounts of soluble materials, such as carbonate cements, embedded in an insoluble matrix. The porosity contrast, defined as the relative increase in porosity across the dissolution front

$$\Delta = \frac{\phi_1 - \phi_0}{\phi_0}, \tag{4.1}$$

is assumed to be small ($\Delta \ll 1$), so that the specific surface area and dispersion tensor can be taken to be constant. More general constitutive relations will be examined in § 6, but we can obtain considerable insight into the interplay of diffusion, dispersion, convection, and reaction from this limiting case.

Although the change in porosity is small, the increase in permeability may be large because of the opening of new flow paths through the rock. The permeability of partially soluble rocks systems is sometimes modelled by an exponential relation $K = K_0 \mathrm{e}^{\alpha(\phi-\phi_0)/\phi_0}$ (Hinch & Bhatt 1990); the permeability gradient (2.27) is then independent of porosity, with $\hat{W} = \hat{W}_0 = \alpha\Delta$. More general models for the permeability of partly soluble rocks, for example (6.12), also reduce to a constant permeability gradient, $\hat{W} \to \hat{W}(\hat{\phi} = 0)$, in the limit of small porosity contrast, $\Delta \ll 1$.

The downstream base solutions for constant surface area ($\hat{s}_b = 1$) and dispersion ($\hat{D}^L_b = \hat{D}^L$) are (3.19)–(3.20)

$$\hat{c}_b = \frac{\mathrm{e}^{-\xi}}{1 + \hat{D}^L}, \quad \hat{\phi}_b = \mathrm{e}^{-\xi}. \tag{4.2}$$

After eliminating the concentration perturbation $f_c = (1 + \hat{D}^L)^{-1} \mathscr{L}_{c\phi} f_\phi$, equation (3.5) can be rewritten as a pair of coupled equations for f_v and f_ϕ:

$$(1 + \hat{D}^L)\mathscr{L}_{vv} f_v + \mathscr{L}_\phi f_\phi = 0, \tag{4.3}$$

$$\mathscr{L}_{\phi v} f_v + \hat{W}_0 \hat{u}^2 f_\phi = 0, \tag{4.4}$$

where $\mathscr{L}_\phi = [\mathscr{L}_{vc}\mathscr{L}_{c\phi} + (1 + \hat{D}^L)\mathscr{L}_{v\phi}]$. Making use of the explicit form for the base solutions (4.2), the operators in (4.3)–(4.4) are simplified:

$$(1 + \hat{D}^L)\mathscr{L}_{vv} = -\mathrm{e}^{-\xi}\left[1 + (\hat{D}^L - \hat{D}^E) - (\hat{D}^T - \hat{D}^E)\partial_\xi\right], \tag{4.5}$$

$$\mathscr{L}_{\phi v} = \partial_\xi^2 - \hat{u}^2 + \hat{W}_0 \mathrm{e}^{-\xi}\partial_\xi, \tag{4.6}$$

$$\mathscr{L}_\phi = \left[\partial_\xi - (\hat{D}^L\partial_\xi^2 - \hat{D}^T\hat{u}^2) + \hat{D}^L + 1\right](\hat{\omega} - \partial_\xi). \tag{4.7}$$

Finally, the boundary conditions at the front, (3.31) and (3.34), can be expressed in terms of f_v and f_ϕ:

$$(\partial_\xi f_v)_0 = \hat{u} f_v(0), \tag{4.8}$$

$$\left[(\hat{\omega} - \partial_\xi)(\partial_\xi - \lambda_c) f_\phi\right]_0 = (1 + \hat{D}^L)\left[\Lambda(0)\left(\lambda_c - \frac{1}{\hat{D}^L} - \hat{u}\right) f_v(0) - \frac{1}{\hat{D}^L} f_\phi(0)\right], \tag{4.9}$$

$$(1 + \hat{D}^L)\Lambda(0) = \frac{\left[\hat{D}^E/\hat{D}^L - \hat{u}(\hat{D}^T - \hat{D}^E)\right]}{\hat{u}\left[1 + \hat{u}(\hat{D}^L - \hat{D}^T)\right]}. \tag{4.10}$$

Equation (4.9) makes use of the relation $f_c = (\hat{\omega} - \partial_\xi) f_\phi/(1 + \hat{D}^L)$ from (3.5) and (3.9), and of the substitution $\xi_0 = f_\phi(0)$ from (3.29) and (4.2). In general, the dispersion tensor in this model is characterized by three constants: $\hat{D}^L \geqslant \hat{D}^T \geqslant \hat{D}^E$. However, in geophysical flows the fluid velocity is usually small and dispersion is then negligible, meaning that $\hat{D}^L = \hat{D}^T = \hat{D}^E$. In such cases $(1 + \hat{D}^L)\mathscr{L}_{vv} \to -\mathrm{e}^{-\xi}$ and $(1 + \hat{D}^L)\Lambda(0) \to \hat{u}^{-1}$.

4.1. *Small permeability gradient:* $\hat{W}_0 \ll 1$

A small porosity contrast does not necessarily imply a small change in permeability. Nevertheless, in the limit that the permeability gradient is small, a regular perturbation expansion around $\hat{W}_0 = 0$ can be made. A similar idea was used in the convective limit by Hinch & Bhatt (1990); details of the extension to include diffusion and dispersion are given in appendix B. Expanding f_v, f_ϕ and $\hat{\omega}$ in powers of $\hat{W}_0$, the growth rate of the instability is given to first order by

$$\hat{\omega} = \hat{\omega}^0 + \hat{W}_0 \hat{\omega}^1 + \cdots. \tag{4.11}$$

The zeroth-order growth rate is always negative,

$$\hat{\omega}^0 = \frac{1 - \sqrt{1 + 4\hat{D}^L \hat{D}^T \hat{u}^2}}{2\hat{D}^L}, \tag{4.12}$$

because a permeability contrast between the dissolved and undissolved material is needed to drive the instability in the reaction front. For small Péclet numbers ($\hat{D}^L \ll 1$) the leading-order contribution to the stabilization of the front is simply $-\hat{D}^T \hat{u}^2$; thus the first correction to the convective limit involves only transverse dispersion (Szymczak & Ladd 2011*b*).

There is a straightforward but lengthy expression for the first-order perturbation in the growth rate (B 14), but it is more instructive to consider various limiting cases.

4.1.1. *Regimes of dissolution*

The growth rate of the instability is a function of wavenumber $\hat{u}$ and four parameters: $\hat{W}_0$, $\hat{D}^L$, $\hat{D}^T$ and $\hat{D}^E$. Here we consider small values of the permeability gradient $\hat{W}_0 \ll 1$ (larger values will be examined in § 4.2) and two velocity regimes: low-velocity dissolution where dispersion is negligible and high velocities where dispersion is important. It is important to emphasize that the transition from convection-dominated to diffusion/dispersion-dominated dissolution is controlled by the reaction rate as well as the velocity (2.23).

4.1.2. *Small velocities:* $\Theta^{L,T} v_0 \ll D^E$

In geophysical flows the fluid velocity is usually small and dispersion can frequently be neglected ($\Theta^{L,T} v_0 \ll D^E$); then all three dispersion coefficients are equal and can

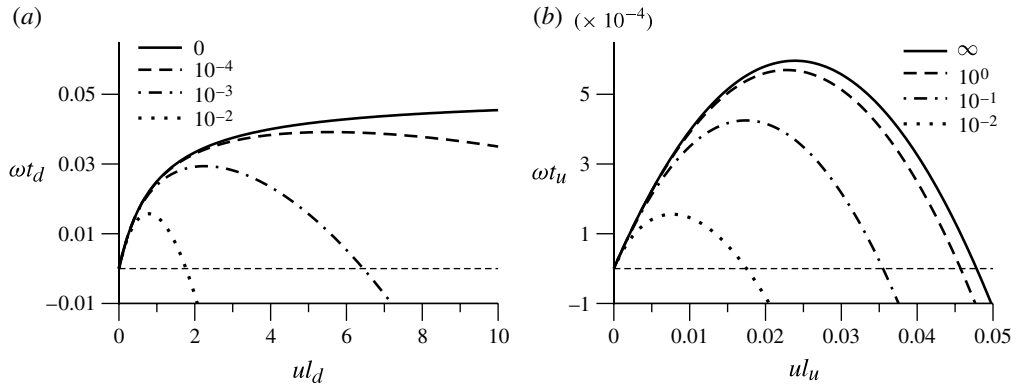

FIGURE 3. Growth rates of the instability in different regimes of convection and diffusion for a small permeability gradient, $\hat{W}_0 = 0.1$. In (*a*) length is scaled by l_d (equation (2.20)), while in (*b*) the diffusive length l_u is used (equation (2.19)). The corresponding dissolution time scales, $t_d = l_d/\gamma_a v_0$ and $t_u = l_u/\gamma_a v_0$, are used to scale the growth rates. The value of H for each curve is indicated in the legend; for $H \ll 1$, $\hat{D} \approx H$ whereas for $H \gg 1$, $\hat{D} \approx H^{1/2}$.

be replaced by a single diffusivity, $\hat{D} = \hat{D}^E = \hat{D}^T = \hat{D}^L$. The dimensionless diffusion coefficient $\hat{D} = (\sqrt{1+4H} - 1)/2$ is equivalent to the inverse of the Péclet number on the scale of the reactant penetration length Pe^{-1} (equation (2.22)). Characteristic dispersion curves ($\hat{\omega}$ versus $\hat{u}$), with $\hat{\omega}^1$ from (B 14), are shown in figure 3 for a small permeability gradient $\hat{W}_0 = 0.1$.

For large Péclet numbers ($\hat{D} \ll 1$), shown in figure 3(*a*), equation (4.11) takes a parabolic limiting form,

$$\hat{\omega} = \frac{\hat{W}_0 \hat{u}}{2(1+\hat{u})} - \hat{D}\hat{u}^2 + \mathscr{O}(\hat{D})^2 \tag{4.13}$$

with results that are indistinguishable from the exact solution of (4.11) on the scale of figure 3. In the convective limit ($H \to 0$), $\hat{\omega} = \omega t_d$ rises monotonically with increasing wavenumber, reaching an asymptotic value $\hat{\omega} = \hat{W}_0/2$ as in Hinch & Bhatt (1990). However, this limit is singular, as indicated by (4.13); even a small amount of dispersion ($H < 10^{-3}$) cuts off the short wavelengths ($\hat{u} = ul_d \gg 1$), leading to a pronounced maximum in the growth rate. This implies that there will be a strong wavelength selection even in highly convective flows and that short wavelength perturbations do not grow. A large permeability gradient $\hat{W}_0 \gg 1$ is needed, in addition to a large flow rate ($H \ll 1$), to overcome the strong stabilizing effect of the zeroth-order (in $\hat{W}_0$) diffusional flux.

As H increases, diffusional stabilization reduces the growth rate and pushes the range of unstable wavelengths towards $\hat{u} = 0$ as can be seen in figure 3(*a*). There is a qualitative change in the length scales illustrated in figure 2; from convection-dominated infiltration, where the downstream penetration length (l_d) is much larger than the upstream length (l_u), to diffusion-dominated infiltration, where the upstream length scale is much larger than the downstream length scale. In the convective limit ($H \to 0$) the concentration at the front is essentially equal to the inlet concentration, whereas in the diffusive limit ($H \to \infty$), the concentration at the front vanishes.

Limiting case	Convection			Diffusion/dispersion		
	$\hat{\omega}_{max}$	$\hat{u}_{max}$	$\hat{u}_{lim}$	$\tilde{\omega}_{max}$	$\tilde{u}_{max}$	$\tilde{u}_{lim}$
$\Theta^{L,T} v_0 \ll D^E$, $H \to 0$	$\dfrac{\hat{W}_0}{2}$	$\left(\dfrac{\hat{W}_0}{4\hat{D}}\right)^{1/3}$	$\left(\dfrac{\hat{W}_0}{2\hat{D}}\right)^{1/2}$			
$\Theta^{L,T} v_0 \ll D^E$, $H \to \infty$				$\dfrac{\hat{W}_0^2}{16}$	$\dfrac{\hat{W}_0}{4}$	$\dfrac{\hat{W}_0}{2}$
$\Theta^{L,T} v_0 \gg D^E$, $H \to 0$	$\dfrac{\hat{W}_0}{2}$	$\left(\dfrac{\hat{W}_0}{4\hat{D}^T}\right)^{1/3}$	$\left(\dfrac{\hat{W}_0}{2\hat{D}^T}\right)^{1/2}$			
$\Theta^{L,T} v_0 \gg D^E$, $H \to \infty$				$\dfrac{\hat{W}_0^2}{16\chi}$	$\dfrac{\hat{W}_0}{4\chi}$	$\dfrac{\hat{W}_0}{2\chi}$

TABLE 2. Summary of limiting cases for a small permeability gradient: expressions for ω_{max}, u_{max} and u_{lim} are shown for convective ($H \to 0$) and diffusive or dispersive ($H \to \infty$) limits. In the first instance the dispersion is purely diffusive ($\Theta^{L,T} = 0$), while in the second case the diffusional contribution is omitted ($\hat{D}^E = 0$); $\chi = \hat{D}^T/\hat{D}^L$ is the ratio of transverse to longitudinal dispersion coefficients in the undisturbed matrix.

If reactive infiltration is diffusion dominated ($H \gg 1$), the dispersion relation (4.11) should be rescaled, replacing the vanishing upstream length l_d (2.20) by $l_u = l_d/\hat{D}$ (2.19) in the length and time scales. This leads to a new dimensionless wavenumber and growth rate,

$$\tilde{u} = \hat{u}\hat{D}, \quad \tilde{\omega} = \hat{\omega}\hat{D}, \tag{4.14}$$

where the new 'diffusive' scaling is indicated by the tilde. Figure 3(*b*) shows that the dispersion relation in this scaling quickly reaches a limiting form for large H,

$$\tilde{\omega} = \frac{\hat{W}_0}{2}\tilde{u} + \left(\frac{1}{2} + \frac{\hat{W}_0}{4}\right)\left(1 - \sqrt{1 + 4\tilde{u}^2}\right), \tag{4.15}$$

shown by the solid line. Equation (4.15) is equivalent to the 'thin-front' limit (Ortoleva *et al.* 1987*a*) for a small permeability gradient. Since $\tilde{u} = u l_u \ll 1$ in the range of positive growth rates (figure 3), a simpler form of (4.15) can be used,

$$\tilde{\omega} = \frac{\hat{W}_0}{2}\tilde{u} - \tilde{u}^2 + \mathcal{O}(\hat{W}_0\tilde{u}^2). \tag{4.16}$$

The key features of the dispersion curves can be summarized by three quantities: the maximum growth rate ω_{max}, the wavenumber characterizing the most unstable mode u_{max} and the largest unstable wavenumber u_{lim}:

$$\left(\frac{\mathrm{d}\omega}{\mathrm{d}u}\right)_{u_{max}} = 0, \quad \omega_{max} = \omega(u_{max}), \quad \omega(u_{lim}) = 0. \tag{4.17}$$

Simple formulas can be found for the various limiting cases and these are summarized in table 2.

4.1.3. *Large velocities:* $\Theta^{L,T} v_0 \gg D^E$

When the flow velocity is sufficiently large, for example during acidization, hydrodynamic dispersion can be more important than molecular diffusion. Here we

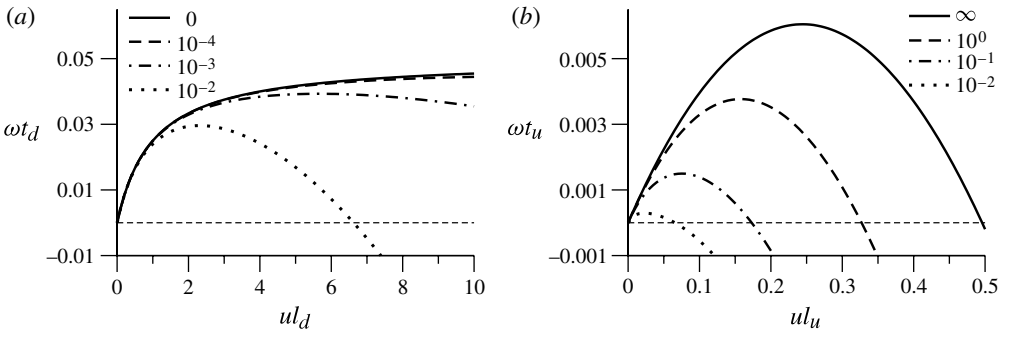

FIGURE 4. Growth rates of the instability in different regimes of convection and dispersion for a small permeability gradient, $\hat{W}_0 = 0.1$; the anisotropy in the dispersion $\chi = \hat{D}^T/\hat{D}^L = 0.1$. The scaling and H values in each panel are the same as in figure 3. Note that the axis scales in the diffusive limit (b) are an order of magnitude larger than in figure 3.

consider a single case where dispersion is dominant, $D^E = 0$, with a 10:1 anisotropy in the dispersion, $\chi = D^T/D^L = 0.1$ and $\hat{W}_0 = 0.1$. The growth rate as a function of $\hat{u}$ is shown in figure 4 for various H values, as in figure 3.

A comparison of figure 4 with figure 3 shows that anisotropic dispersion leads to systematically larger growth rates over the whole range of H because the zeroth-order stabilization is smaller (4.12). The asymptotic expansion in the convective limit ($H \to 0$) takes the same form as (4.13);

$$\hat{\omega} = \frac{\hat{W}_0 \hat{u}}{2(1+\hat{u})} - \hat{D}^T \hat{u}^2. \tag{4.18}$$

Here transverse dispersion is the controlling parameter, while $\hat{D}^L$ disappears altogether, even from the length scale $l_d \to v_0/ks_0$ (equation (2.20)). The shape of the dispersion curve, the location of the maximum growth rate $\hat{u}_{max}$ and the crossing point $\hat{u}_{lim}$, are functions of a single parameter $\hat{W}_0/\hat{D}^T$. In the dispersive limit ($H \to \infty$, $\hat{D}^E = 0$) the growth rate is similar to (4.16) (again for small $\hat{W}_0$); after rescaling as in (4.14),

$$\tilde{\omega} = \frac{\hat{W}_0}{2}\tilde{u} - \chi \tilde{u}^2. \tag{4.19}$$

Other terms are small in the range of positive growth rates, since $\tilde{u}_{lim}$ is proportional to $\hat{W}_0$ in the first approximation. Expressions for ω_{max}, u_{max} and u_{lim} in dispersive infiltration are given in table 2.

4.2. *Finite permeability gradient:* $\hat{W}_0 > 1$

When there is significant permeability gradient ($\hat{W}_0 > 1$), the growth rate must be determined numerically. We used a spectral method, described in appendix C, to calculate dispersion curves for $\hat{W}_0 = 10$, corresponding to a permeability contrast $\hat{K}_1 \approx 22\,000$. The growth rates of the instability in the absence of hydrodynamic dispersion ($\Theta^{L,T} v_0 \ll D^E$) are shown in figure 5. In contrast with the small permeability gradient data in figure 3, here the convective region is extended and larger H values are needed to stabilize the smaller wavelengths. The approach to the diffusive limit is no longer monotonic in the upstream scaling (4.14); the dispersion

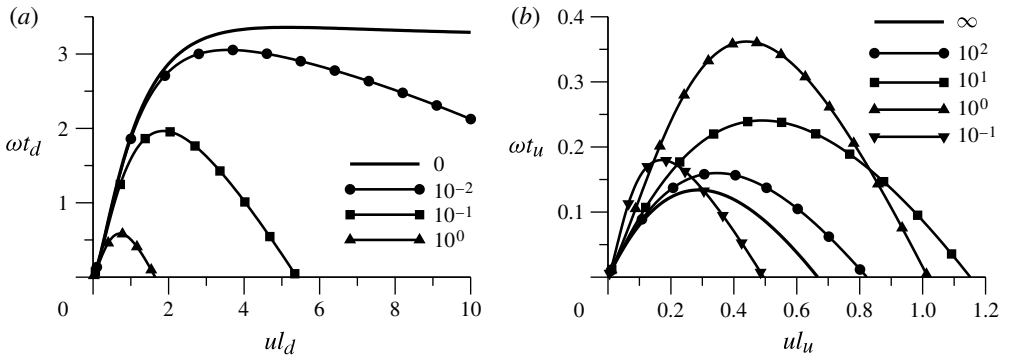

FIGURE 5. Growth rates of the instability in different regimes of convection and dispersion for a permeability gradient, $\hat{W}_0 = 10$, and equal dispersion coefficients $\hat{D}^L = \hat{D}^T = \hat{D}^E$. The scaling in each panel is the same as in figure 3.

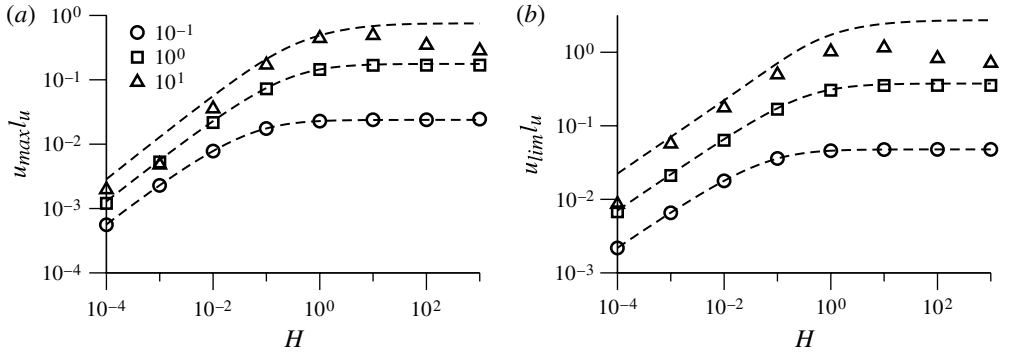

FIGURE 6. (*a*) The maximally unstable wavenumber, $\tilde{u}_{max} = u_{max}v_0/D$, and (*b*) the largest unstable wavenumber, $\tilde{u}_{lim} = u_{lim}v_0/D$, are shown as a function of H at different values of the permeability gradient: $\hat{W}_0 = 0.1$ (circles), $\hat{W}_0 = 1$ (squares) and $\hat{W}_0 = 10$ (triangles). The dashed lines are the linear theory (4.11): $\hat{W}_0 = 0.1$ (bottom), $\hat{W}_0 = 1$ (middle) and $\hat{W}_0 = 10$ (top).

curves approach the asymptotic ($H \to \infty$) limit from above, whereas in figure 3 they approach from below.

In figure 6 the dimensionless wavectors in the upstream scaling, $\tilde{u}_{max} = u_{max}l_u$ and $\tilde{u}_{lim} = u_{lim}l_u$, are shown for different values of the permeability gradient $\hat{W}_0$. In diffusion-dominated dissolution ($H \gg 1$), the dispersion relation approaches a limiting form (5.1), which is independent of H (Chadam *et al.* 1986). As the velocity increases, convection starts to play a role and the dominant length scale shifts to the downstream (reactant) length. Equation (4.13) shows that at small H, $\tilde{u}_{max} \sim (\hat{W}_0 H^2/4)^{1/3}$ for sufficiently small $\hat{W}_0$. The first-order theory gives an accurate representation of $\tilde{u}_{max}$, $\tilde{u}_{lim}$ and $\tilde{\omega}_{max}$ for permeability gradients up to $\hat{W}_0 = 1$. However, when the permeability gradient is high ($\hat{W}_0 = 10$) the power-law scaling of $\hat{u}_{max}$ in convection-dominated dissolution ($H \ll 1$) is no longer observed.

5. Thin-front limit

Reactive infiltration of a porous material is unstable even when the diffusive or dispersive flux is significant, as can be seen in figures 3–5(*b*). Here we investigate the thin-front limit first analysed by Chadam *et al.* (1986), but without assuming that $\hat{W}_0$ is small as was the case in § 4.1. Taking into account the different scaling relations, their dispersion equation, e.g. VIII.3 of Ortoleva *et al.* (1987*a*), reads (in our notation)

$$\tilde{w} = \frac{1}{1+\Gamma}\left[(1-\Gamma)\tilde{u} + 1 - \sqrt{1+4\tilde{u}^2}\right]; \tag{5.1}$$

here we have used the upstream scaling (4.14), because the downstream length is vanishing in the diffusive limit. The coefficient Γ is the permeability contrast,

$$\Gamma = \frac{K_0}{K_1}; \tag{5.2}$$

for the exponential permeability model (§ 4) $\Gamma = \mathrm{e}^{-\hat{W}_0}$. In making these connections it should be noted that Ortoleva *et al.* (1987*a*) define the permeability in terms of the average fluid velocity in the pores, rather than the superficial velocity. In addition they use a rescaled (but still dimensional) time scale equal to $\Delta\gamma_a t$. We will show below that their result (5.1) follows from our equations in the limit $H \to \infty$. The essential approximation in the thin-front limit is that the downstream penetration length can be neglected, so that the porosity field is a step change at the front. Wangen (2013) assumes a step change in all of the fields, including concentration, which is equivalent to a long-wavelength (small $\tilde{u}$) expansion of (5.1).

For large H the upstream penetration length is much longer than the downstream length, $l_u \gg l_d$. If we take $l_u = D_1^L \phi_1 / v_0$ (figure 2) as the characteristic length scale, then the base concentration profiles in the limit $H \to \infty$ are, from (3.21) and (3.22),

$$\hat{c}_b^u(\zeta < 0) = 1 - \mathrm{e}^{\zeta}, \quad \hat{c}_b(\zeta > 0) = 0, \tag{5.3}$$

where $\zeta = x'/l_u$ (equation (4.14)). The base concentration field vanishes at the front, because on the scale of l_u, all of the reactant is consumed in an infinitesimal region at the front itself. The porosity field is constant throughout the matrix, with a jump condition at the front accounting for the dissolved material,

$$\hat{\phi}(\zeta < \zeta_f) = 1, \quad \hat{\phi}(\zeta > \zeta_f) = 0. \tag{5.4}$$

Similarly, the concentration gradient and tangential velocity are also discontinuous across the front. Nevertheless, continuity of concentration and reactant flux leads to a boundary condition on f_c, while the boundary condition on f_v follows from continuity of pressure and normal velocity. Here we just quote the results, which are derived in appendix D:

$$f_c^u(0) = \zeta_0, \quad (\partial_\zeta f_c^u)_0 = \zeta_0(1-\tilde{\omega}) + (1-\tilde{D}_1^E) f_v^u(0), \quad f_v^u(0) = \zeta_0 \tilde{u}\left(\frac{1-\Gamma}{1+\Gamma}\right), \tag{5.5}$$

where Γ is the permeability contrast (5.2) and ζ_0 is the amplitude of the perturbation.

The upstream perturbations in concentration and velocity (3.12), after rescaling length by l_u instead of l_d, are given by

$$\mathrm{e}^{\zeta}\left[(\tilde{D}_1^T - \tilde{D}_1^E)\partial_\zeta - \tilde{D}_1^E\right] f_v + \left[\partial_\zeta - \partial_\zeta^2 + \tilde{D}_1^E \tilde{u}^2\right] f_c = 0, \tag{5.6}$$

$$\left[\partial_\zeta^2 - \tilde{u}^2\right] f_v = 0, \tag{5.7}$$

where $\tilde{D}_1^L = 1$ in this scaling. The solutions satisfying the upstream ($\zeta \to -\infty$) boundary conditions are

$$f_v^u = A_v \mathrm{e}^{\tilde{u}\zeta}, \quad f_c^u = A_c \mathrm{e}^{\lambda_c^u \zeta} - A_v \Lambda^u(\zeta), \tag{5.8}$$

where λ_c^u and $\Lambda^u(\zeta)$ are equivalent to λ_c (3.26) and $\Lambda(\xi)$ (3.27) in the upstream scaling:

$$\lambda_c^u = \frac{1 + \sqrt{1 + 4\tilde{D}_1^T \tilde{u}^2}}{2}, \quad \Lambda^u(\zeta) = \frac{\left[\tilde{D}_1^E - \tilde{u}(\tilde{D}_1^T - \tilde{D}_1^E)\right]}{\tilde{u}\left[1 + \tilde{u}(1 - \tilde{D}_1^T)\right]} \mathrm{e}^{(1+\tilde{u})\zeta}. \tag{5.9}$$

Substituting these solutions into the boundary conditions (5.5) eliminates A_v and A_c, and determines the growth rate in the thin-front limit:

$$\tilde{\omega} = \tilde{\omega}^0 + \left(\frac{1 - \Gamma}{1 + \Gamma}\right)\left[(1 - \tilde{D}_1^E)\tilde{u} + (\tilde{u} + \tilde{\omega}^0)\tilde{u}\Lambda^u(0)\right], \tag{5.10}$$

where $\tilde{\omega}^0 = 1 - \lambda_c^u$ is the (negative) growth rate in the absence of a permeability contrast, cf. (4.12),

$$\tilde{\omega}^0 = \frac{1 - \sqrt{1 + 4\tilde{D}_1^T \tilde{u}^2}}{2}. \tag{5.11}$$

It can be verified that, for a small permeability gradient $\Gamma \approx 1 - W_0$, (5.10) coincides with the small Péclet limit of (4.11) with $\hat{\omega}^1$ given by (B 14). Equation (5.10) also agrees with (4.2) of Chadam *et al.* (2001), after accounting for the different scaling of the variables.

We next consider the same two limiting cases as in § 4.1: small velocities $\Theta_0^{L,T} v_0 \ll D_0^E$ and large velocities $\Theta_0^{L,T} v_0 \gg D_0^E$. The thin-front limit can occur for both diffusion-dominated and dispersion-dominated infiltration.

5.1. *Small velocities:* $\Theta_1^{L,T} v_0 \ll D_1^E$

When dispersion is negligible and all three coefficients are the same, then in the upstream scaling $\tilde{D}_1^E = \tilde{D}_1^T = 1$ and $\Lambda^u(0) = \tilde{u}^{-1}$. Then we recover the simple formula for the growth rate of the instability given in (5.1). However, equation (5.1) only gives the correct dispersion curve in the limit $H \to \infty$ (and $\gamma_a \to 0$). The values for $\tilde{u}_{max}$ and $\tilde{u}_{lim}$ derived from (5.1),

$$\tilde{u}_{max} = \frac{1 - \Gamma}{2\sqrt{3 + 2\Gamma - \Gamma^2}}, \quad \tilde{u}_{lim} = \frac{2(1 - \Gamma)}{3 + 2\Gamma - \Gamma^2}, \tag{5.12}$$

are not generally applicable, but only in the diffusive (or thin-front) limit.

5.2. *Large velocities:* $\Theta_0^{L,T} v_0 \gg D_0^E$

When hydrodynamic dispersion is dominant, the growth rate depends on the ratios of dispersion coefficients, $\tilde{D}_1^E < \tilde{D}_1^T < 1$, as well as the wavenumber $\tilde{u}$. We examined the case of a small permeability contrast ($\Gamma \approx 1$) in § 4.1.3; here we focus on high permeability contrasts, taking the limiting case $\Gamma = 0$ in (5.10) as an example. Figure 7(*a*) shows that isotropic dispersion ($\tilde{D}_1^E \ll 1, \tilde{D}_1^T = 1$) gives similar growth rates to pure diffusion ($\tilde{D}_1^E = 1$), because the upstream scaling in figure 7 ($l_u = D_1^L / v_0$) leads to a velocity-independent base state (5.3) in the scaled variables. The dimensional reactant penetration length l_u varies from D_1^E / v_0 (pure diffusion)

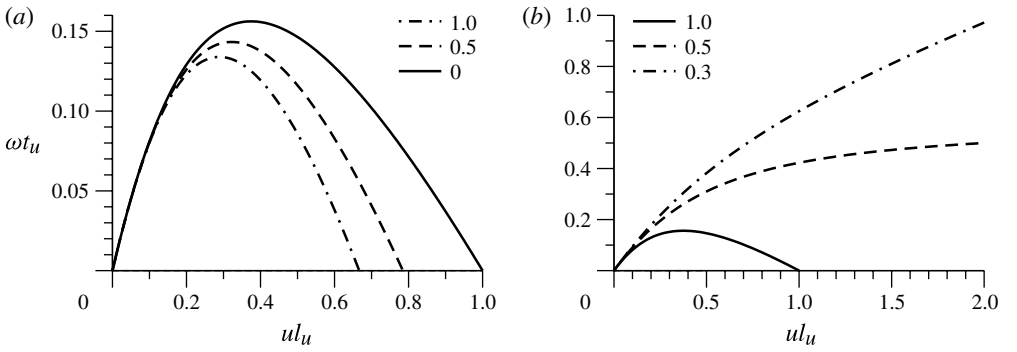

FIGURE 7. Growth rates of the instability in the thin-front ($H \to \infty$) limit with a large permeability contrast, $\Gamma = 0$: (*a*) the differences between isotropic dispersion and diffusion, where the diffusive term $\tilde{D}_1^E = D_1^E/D_1^L$ varies between 0 and 1 while $\tilde{D}_1^T = D_1^T/D_1^L = 1$, with $\tilde{D}_1^E = 1$ (solid line), $\tilde{D}_1^E = 0.5$ (dashed line) and $\tilde{D}_1^E = 0$ (dot-dashed line); (*b*) the effects of anisotropic dispersion when the diffusive contribution is negligible ($\tilde{D}_1^E = 0$), with $\tilde{D}_1^T = 1$ (solid line), $\tilde{D}_1^T = 0.5$ (dashed line) and $\tilde{D}_1^T = 0.3$ (dot-dashed line). Length and time are scaled by the upstream length (l_u) and time (t_u) scales.

to Θ_1^L (pure dispersion). Results for a weak permeability contrast are similar to figures 1 and 2 of Chadam *et al.* (2001), after noting that they plot the growth rate against the dimensional wavenumber u rather than $\tilde{u}$.

Figure 7(*b*) shows that the growth rate is sensitive to anisotropy in the dispersion; we again take $\Gamma = 0$, which is typical of carbonate dissolution (for example), and $\tilde{D}_1^E = 0$, meaning that diffusion in the fully dissolved matrix is negligible. The solid line ($\tilde{D}_1^T = 1$) indicates isotropic dispersion and corresponds to the solid line in Figure 7(*a*). However, when transverse dispersion is small ($\tilde{D}_1^T = 0.3$), short-wavelength modes are destabilized and the growth rate increases linearly with $\tilde{u}$; the transition between stable short wavelengths and an unbounded growth rate occurs at $\tilde{D}_1^T = 1/2$. Figure 3 of Chadam *et al.* (2001) shows a much smaller permeability contrast ($\Gamma = 0.85$) where short wavelengths are always stable (§ 4.1).

The boundary between stable and unstable short-wavelength modes is illustrated in figure 8, which shows the transition value of $\tilde{D}_1^T$ as a function of Γ for various values of $\tilde{D}_1^E$. There is a limitation on the possible values of $\tilde{D}_1^E$ imposed by the condition of positive dispersion $\tilde{D}_1^T > \tilde{D}_1^E$. When dispersion is significant $\tilde{D}_1^E < 0.3$ we can expect unstable short-wavelength modes whenever there is significant permeability contrast $\Gamma < 0.2$. For example, dissolution of cemented sandstone causes permeability increases of one to two orders of magnitude (Fogler & McCune 1976), corresponding to $0.01 < \Gamma < 0.1$. It is not clear what the stabilizing mechanism would be in such cases, but it does not seem to arise from a macroscopic transport theory.

Dispersion-dominated dissolution can be further investigated by examining the behaviour at small and large $\tilde{u}$. At small $\tilde{u}$ the growth rate,

$$\tilde{w} = \frac{1}{1+\Gamma}\left[(1-\Gamma)\tilde{u} - 2\tilde{D}_1^T\tilde{u}^2\right] + \mathcal{O}(\tilde{u}^4), \tag{5.13}$$

shows that the stabilizing term is controlled by $\tilde{D}_1^T$ as in (4.19). On the other hand, at sufficiently large wavenumbers the growth rate is proportional to wavenumber

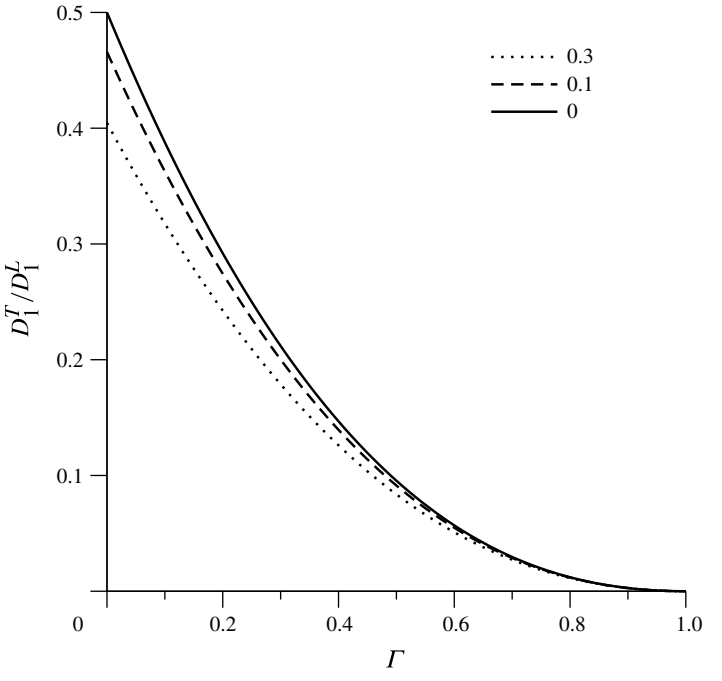

FIGURE 8. Boundary between stable and unstable growth at short wavelengths. The lines indicate the separation in the $\Gamma - \tilde{D}_1^T$ plane between regions where shorter wavelengths are increasingly unstable (below the line) and regions where short wavelengths are stable (above the line). The different lines are for different levels of diffusion: $\tilde{D}_1^E = 0$ (solid line), $\tilde{D}_1^E = 0.1$ (dashed line) and $\tilde{D}_1^E = 0.3$ (dot-dashed line).

(5.10), $\tilde{\omega}(\tilde{u} \to \infty) \to C\tilde{u}$, with a coefficient

$$C = \left(\frac{1-\Gamma}{1+\Gamma}\right)\left(1 - \tilde{D}_1^E - \frac{\tilde{D}_1^T - \tilde{D}_1^E}{1+\sqrt{\tilde{D}_1^T}}\right) - \sqrt{\tilde{D}_1^T}, \tag{5.14}$$

which can be either positive or negative. When diffusion dominates over dispersion (§ 5.1) $\tilde{D}_1^E \approx \tilde{D}_1^T \approx 1$ (or $D_1^E \approx D_1^T \approx D_1^L$) and C is always negative. However, when there is anisotropic dispersion, the large $\tilde{u}$ growth rate can be positive, and in this case the short-wavelength modes are the *least* stable.

6. Convective limit: $H \to 0$

The opposite limit to that considered in § 5 arises when diffusion is negligible ($H \to 0$); here the upstream length (l_u) vanishes in comparison to the downstream length $l_d = v_0/ks_0$ and the inlet concentration is maintained right up to the front, $\hat{c}_b(0) = 1$. The base porosity fields, (3.19) and (3.20), then follow from a single differential equation

$$\partial_\xi \hat{c}_b = \partial_\xi \hat{\phi}_b = -\hat{s}_b \hat{\phi}_b, \tag{6.1}$$

where the reactive surface area $\hat{s}_b$ is a function of porosity. We will use the convective limit to examine the consequences of different models for permeability and reactive

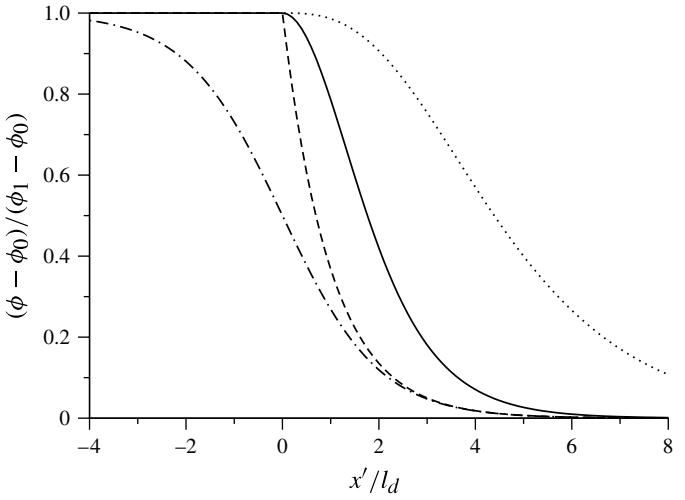

FIGURE 9. Steadily propagating (base) porosity profiles: dashed line, constant specific surface area (6.14); dashed-dot line, powder model (6.15); solid line, grain model (6.16); and dotted line, spherical grain model $\hat{s} = (1 - \hat{\phi})^{2/3}$.

surface area, making use of the simplifications that follow from ignoring diffusion and dispersion. This will also allow us to connect our results to previous work (Sherwood 1987; Hinch & Bhatt 1990).

6.1. *Equations and boundary conditions*

In the absence of diffusion, the equations for the perturbed fields (3.5) are

$$(\partial_\xi \hat{c}_b) f_v + \partial_\xi f_c + (\hat{\omega} - \partial_\xi) f_\phi = 0, \tag{6.2}$$

$$-\hat{s}_b f_c + (\hat{\omega} - \partial_\xi - \hat{s}_b' \hat{c}_b) f_\phi = 0, \tag{6.3}$$

$$\left[\partial_\xi^2 - \hat{W}_b(\partial_\xi \hat{\phi}_b)\partial_\xi - \hat{u}^2\right] f_v + \hat{W}_b \hat{u}^2 f_\phi = 0. \tag{6.4}$$

In convection-dominated dissolution, there is usually a well-defined front behind which the material is fully dissolved (figure 9); the powder model with its diffuse base profile will be considered separately (§ 6.4). In all other cases the concentration matching conditions at the front (3.17) can be replaced by a Dirichlet condition $\hat{c}(\xi_f) = 1$. The base solutions then satisfy the boundary conditions $\hat{\phi}_b(0) = \hat{c}_b(0) = 1$, while the boundary conditions on the perturbations are

$$f_\phi(0) = \xi_0(-\partial_\xi \hat{\phi}_b)_0, \tag{6.5}$$

$$f_c(0) = \xi_0(-\partial_\xi \hat{c}_b)_0, \tag{6.6}$$

$$(\partial_\xi f_v)_0 = \hat{u} f_v(0). \tag{6.7}$$

If the permeability of the fully dissolved state $\hat{W}(\hat{\phi} \to 1)$ diverges, as in (6.10) and (6.13), there is no pressure gradient upstream of the front. The continuity of the flow field (6.7) must then be replaced by a constant pressure at the front $\hat{p}(\xi_f) = \hat{p}_{in}$. In

terms of the pressure perturbation $\delta\hat{p} = f_p(\xi)\mathrm{e}^{\hat{\omega}\tau}\cos(\hat{u}\eta)$,

$$f_p(0) = -\xi_0(\partial_\xi \hat{p}_b)_0 = -\frac{\xi_0}{\hat{K}_1}, \tag{6.8}$$

where the base pressure in the downstream region is given $\hat{p}(\xi) = \hat{p}_0 + \int_0^\xi \hat{K}^{-1}(\xi')\,\mathrm{d}\xi'$. The transverse velocity at the front, $\hat{v}_\eta = \hat{K}_1\partial_\eta\delta\hat{p}$ can be used to link $(\partial_\xi f_v)_0$ and $f_p(0)$ via the incompressibility condition (3.4),

$$(\partial_\xi f_v)_0 = \hat{K}_1\hat{u}^2 f_p(0) = -\xi_0\hat{u}^2, \tag{6.9}$$

which replaces (6.7) as the boundary condition on f_v.

6.2. *Constitutive models*

We have adopted several different models for permeability and specific surface area in order to facilitate comparisons with previous work.

6.2.1. *Permeability*

The permeability enters into the theory of the instability via its logarithmic derivative $\hat{W}$ (equation (2.27)). Permeability models can be compared based on their gradient, which we define in terms of the undissolved material $\hat{W}_0 = \hat{W}(\hat{\phi} = 0)$.

(i) Inverse solids fraction (ISF):

$$K = K_0\left(\frac{1-\phi_0}{1-\phi}\right) = \frac{K_0}{1-\hat{\phi}}, \quad \hat{W}(\hat{\phi}) = \frac{1}{1-\hat{\phi}}, \quad \hat{W}_0 = 1. \tag{6.10}$$

This is a simple model of a fully soluble material (taking $\phi_1 = 1$); we use it to compare with Sherwood (1987).

(ii) Exponential (EXP):

$$K = K_0\exp\left[\alpha\left(\frac{\phi-\phi_0}{\phi_0}\right)\right] = K_0\mathrm{e}^{\alpha\Delta\hat{\phi}}, \quad \hat{W}(\hat{\phi}) = \alpha\Delta, \quad \hat{W}_0 = \alpha\Delta. \tag{6.11}$$

The EXP model is sometimes used to model clay or limestone-filled rocks, where a small increase in porosity can lead to a large increase in permeability. In § 4 we made use of the simplifications arising from a constant $\hat{W}$; here we use the model to compare with Hinch & Bhatt (1990).

(iii) Carman–Kozeny with constant surface area (CKS), $K \propto \phi^3$:

$$K = K_0\left(\frac{\phi}{\phi_0}\right)^3 = K_0(1+\Delta\hat{\phi})^3, \quad \hat{W}(\hat{\phi}) = \frac{3\Delta}{1+\Delta\hat{\phi}}, \quad \hat{W}_0 = 3\Delta. \tag{6.12}$$

The Carman–Kozeny model, $K \propto \phi^3/s^2$, is a standard model for the permeability of soluble rocks; $\Delta = (\phi_1 - \phi_0)/\phi_0$ is the porosity contrast (4.1), and the specific surface area is assumed to be constant.

(iv) Carman–Kozeny with a grain model for the surface area (CKG), $K \propto \phi^3/(1-\phi)$:

$$K = K_0\frac{(1+\Delta\hat{\phi})^3}{(1-\hat{\phi})}, \quad \hat{W}(\hat{\phi}) = \frac{3\Delta}{1+\Delta\hat{\phi}} + \frac{1}{1-\hat{\phi}}, \quad \hat{W}_0 = 3\Delta + 1. \tag{6.13}$$

In this version of the Carman–Kozeny permeability we use (6.16) to calculate the specific surface area, $s \propto (1-\phi)^{1/2}$. The functional form is different from the

standard Carman–Kozeny equation, $K \propto \phi^3/(1-\phi)^2$, which assumes the porosity depends on the number density of grains rather than the variation in grain size.

The ISF and CKG models apply to fully soluble rocks such as limestone or gypsum, whereas EXP and CKS apply to partially soluble rocks, such as clay or limestone embedded in an insoluble quartz matrix.

6.2.2. *Specific surface area*

We have investigated the convective instability for three different models of the specific surface area, described in (6.14)–(6.16); the base porosity profiles from (6.1) are illustrated in figure 9 along with a numerical solution of the porosity profile from the spherical grain model.

(i) Constant surface area: this is the simplest model to analyse. It has the drawback that the dissolution rate is non-zero at $\phi = \phi_1$:

$$s = s_0, \quad \hat{s} = 1, \quad \hat{c}_b = \hat{\phi}_b = \mathrm{e}^{-\xi}. \tag{6.14}$$

(ii) Powder model: we use this model to compare with Hinch & Bhatt (1990), who assume the reaction rate is proportional to the volume of solid rather than its surface area. It has the disadvantage that the there is not a sharply defined front. Taking the exponential model for the permeability (6.11),

$$s \propto \phi_1 - \phi, \quad \hat{s} = 1 - \hat{\phi}, \quad \hat{c}_b = \hat{\phi}_b = \frac{1}{1+\mathrm{e}^{\xi}}. \tag{6.15}$$

There is an arbitrary choice of origin in the expression for the porosity and concentration profiles; we take $\xi = 0$ as the median position, $\hat{\phi}_b(0) = \hat{c}_b(0) = 1/2$.

(iii) Grain model: the evolving surface area of granular pores can be approximated by power-law models $\hat{s} = (1-\hat{\phi})^q$ (Noiriel, Gouze & Bernard 2004; Noiriel *et al.* 2009); a well-defined front is formed when $q < 1$, with $\hat{\phi} = 1$ in the region behind the front ($\xi < \xi_f$). If the grains are assumed to be spherical and fully exposed (Ortoleva *et al.* 1987*a*), then $q = 2/3$, but in this case the downstream base profiles cannot be calculated explicitly. We use $q = 1/2$ for the instability analysis because it has the same qualitative porosity profile as the $q = 2/3$ model (figure 9), with a well-defined front and a vanishing slope at $\xi = 0$:

$$s \propto (1-\phi)^{1/2}, \quad \hat{s} = (1-\hat{\phi})^{1/2}, \quad \hat{c}_b = \hat{\phi}_b = \mathrm{sech}^2(\xi/2). \tag{6.16}$$

6.3. *Constant surface area:* $\hat{s} = 1$

If the specific surface area is constant during dissolution, equations (6.3)–(6.4) can be used to eliminate f_c and f_v from (6.2), which then reduces to a single equation for the perturbation in the porosity field,

$$\left(\hat{W}_b^{-1}\partial_\xi^2 + \mathrm{e}^{-\xi}\partial_\xi - \hat{W}_b^{-1}\hat{u}^2\right)\mathrm{e}^{\xi}(\partial_\xi + 1)(\partial_\xi - \hat{\omega})f_\phi - \hat{u}^2 f_\phi = 0. \tag{6.17}$$

The equation for f_ϕ was recast in terms of $\hat{W}_b^{-1}$ to take care of cases where the permeability diverges at the front), such as the ISF model (6.10). Similarly, the boundary conditions at the front, equations (6.5)–(6.7) can be reduced to a set of three boundary conditions on f_ϕ (with $\phi_b = \hat{c}_b = \mathrm{e}^{-\xi}$):

$$f_\phi(0) = \xi_0, \quad (\partial_\xi f_\phi)_0 = (\hat{\omega} - 1)f_\phi(0), \quad \left[(\partial_\xi - \hat{u} + 1)(\partial_\xi + 1)(\partial_\xi - \hat{\omega})f_\phi\right]_0 = 0, \tag{6.18}$$

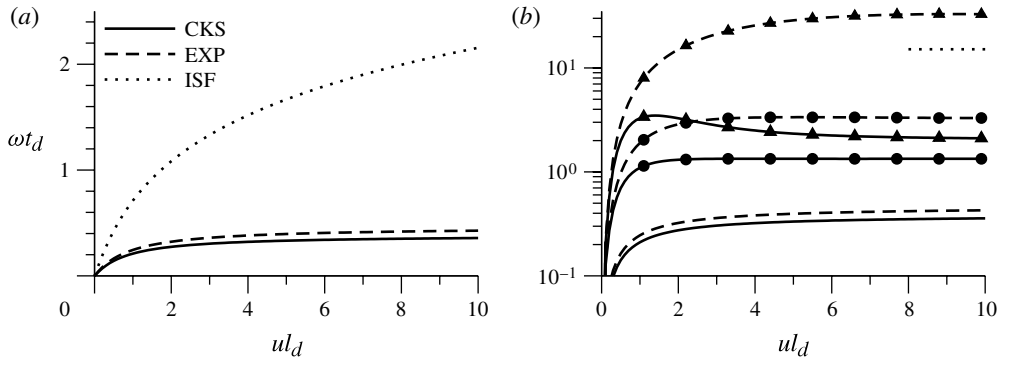

FIGURE 10. Dispersion curves in the convective limit ($H \to 0$) at constant specific surface area, $\hat{s} = 1$, as calculated by the spectral method from appendix C. (*a*) The growth rates for the ISF (6.10), EXP (6.11) and CKS (6.12) permeability relations; in each case $\hat{W}_0 = 1$. (*b*) Growth rates for the EXP (dashed lines) and CKS (solid lines) permeability models with $\hat{W}_0 = 1$ (lines), $\hat{W}_0 = 10$ (circles) and $\hat{W}_0 = 100$ (triangles). The dotted line is the asymptotic value for the EXP model with $W_0 = 100$; the other asymptotes are indistinguishable from their values at $ul_d = 10$ on the scale of the graph.

or, in the case of a diverging permeability (6.10),

$$f_\phi(0) = \xi_0, \quad (\partial_\xi f_\phi)_0 = (\hat{\omega} - 1) f_\phi(0), \quad \left[(\partial_\xi + 1)^2 (\partial_\xi - \hat{\omega}) f_\phi\right]_0 - \hat{u}^2 f_\phi(0) = 0. \quad (6.19)$$

We have calculated dispersion relations for different models of the permeability-porosity relation, ISF, EXP and CKS, using the spectral method described in appendix C.

Equation (6.17) was first derived by Sherwood (1987), using an explicit form for the permeability equivalent to (6.10); the differential equation is now only fourth order, one less than in cases with diffusion. We have verified that the dispersion relation and boundary conditions in Sherwood's paper reduce to (6.17) and (6.19) in the limit of small acid capacity number, $\gamma_a \to 0$. Figure 3 of Sherwood's paper shows that the primary effect of acid capacity number is accounted for in the time scale (2.25). The diverging permeability in the ISF model leads to a logarithmically increasing growth rate at large values of $\hat{u}$ (Sherwood 1987), in contrast to the constant asymptotic growth rate in cases where the permeability remains finite (Hinch & Bhatt 1990), as illustrated in figure 10(*a*). However, for finite Péclet numbers the much stronger diffusive stabilization, proportional to $\hat{u}^2$, will quickly overwhelm the diverging convective contribution.

When the permeability contrast is bounded (e.g. CKS and EXP permeability models in figure 10), the growth rate tends to a constant value at large $\hat{u}$. For small permeability gradients ($\hat{W}_0 < 1$) the growth rate increases monotonically with $\hat{u}$, but for larger $\hat{W}_0$ there is a peak growth rate followed by a slow decay to the asymptotic value (Szymczak & Ladd 2011*b*). The peak is quite noticeable in the case of the CKS model with $\hat{W}_0 = 100$ (solid line + triangles) but it is present in the EXP model as well, most clearly when $\hat{W}_0 = 100$; the asymptotic value from the largest root of (E 3) is shown by the dotted line. Dissolution of porous materials can therefore show wavelength selection in the convective limit if the porosity contrast is sufficiently large, similar to the case of fracture dissolution (Szymczak & Ladd 2011*b*, 2012).

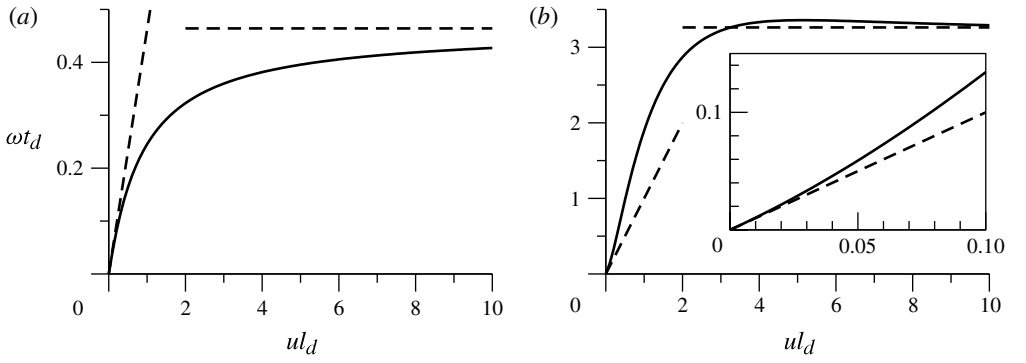

FIGURE 11. Dispersion curves for the exponential permeability model with $H = 0$ and $\hat{s} = 1$. The dashed lines indicate the asymptotic values of $\hat{\omega} t_d$ at large and small wavelengths. Results are shown for $\hat{W}_0 = 1$ (*a*) and $\hat{W}_0 = 10$ (*b* and the inset).

In the convective limit, the growth rates at small wavelengths can be obtained from asymptotic analysis (Hinch & Bhatt 1990), as described in appendix E, while for sufficiently long wavelengths the thin-front limit (5.1) is valid (Wangen 2013). The limiting solutions for a constant permeability gradient $\hat{W} = \hat{W}_0$ are compared with results from the spectral code in figure 11. The growth rate increases to a plateau value, $\hat{\omega}_\infty = \hat{\omega}(\hat{u} \to \infty)$, which is always positive and is equal to the largest root of (E 3). For small permeability gradient, the plateau value is linear in $\hat{W}_0$, $\hat{\omega}_\infty \approx \hat{W}_0/2$ (equation (4.13)), but as $\hat{W}_0$ increases, the asymptotic growth rate increases more slowly, roughly as $\hat{W}_0^{1/2}$. At long wavelengths the growth rate increases linearly, with a slope of $(1 - \Gamma)/(1 + \Gamma)$ (5.1), but at higher permeability gradients ($\hat{W}_0 \gg 1$) the asymptotic regime is only reached at the longest wavelengths (see the inset to figure 11).

6.4. *Powder model*

A perturbative scheme similar to that used in § 4.1 was introduced previously by Hinch & Bhatt (1990), assuming the reaction rate was proportional to the volume fraction of the solid; mathematically this is equivalent to the powder model for the specific surface area $\hat{s} = 1 - \hat{\phi}$. This model is somewhat simpler to analyse than the grain model (§ 6.5) because the specific surface area is an analytic function of $\hat{\phi}$, but it does not lead to a well-defined front (figure 9). From (6.2)–(6.4), together with (6.15) for the base profiles and the exponential model for the permeability (6.11):

$$\frac{-\mathrm{e}^{\xi}}{(1+\mathrm{e}^{\xi})^2} f_v = (\partial_\xi - \hat{\omega}) f_\phi - \partial_\xi f_c, \tag{6.20}$$

$$\frac{\mathrm{e}^{\xi}}{1+\mathrm{e}^{\xi}} f_c = (-\partial_\xi + \frac{1}{1+\mathrm{e}^{\xi}} + \hat{\omega}) f_\phi, \tag{6.21}$$

$$\hat{W}_0 \hat{u}^2 f_\phi = (-\partial_\xi^2 + \hat{W}_0 \frac{-\mathrm{e}^{\xi}}{(1+\mathrm{e}^{\xi})^2} \partial_\xi + \hat{u}^2) f_v. \tag{6.22}$$

Equations (6.20)–(6.22) are equivalent to those of Hinch & Bhatt (1990) in the limit of small acid capacity number.

The first-order growth rate is (Hinch & Bhatt 1990)

$$\hat{\omega}^1 = -\int_{-\infty}^{\infty} \frac{\mathrm{e}^{\xi}}{(1+\mathrm{e}^{\xi})^2} f_v^1 \,\mathrm{d}\xi, \tag{6.23}$$

where the first-order perturbation to the velocity field is given by

$$(\partial_\xi^2 - \hat{u}^2) f_v^1 = \frac{\hat{u}^2 \mathrm{e}^{\xi}}{(1+\mathrm{e}^{\xi})^2}, \tag{6.24}$$

with boundary conditions $f_v^1(\xi \to \pm\infty) \to 0$:

$$f_v^1 = -\frac{u}{2}\left[\int_{\xi}^{\infty} \mathrm{e}^{u(\xi-\xi')} \frac{\mathrm{e}^{\xi'}}{(1+\mathrm{e}^{\xi'})^2}\,\mathrm{d}\xi' + \int_{-\infty}^{\xi} \mathrm{e}^{-u(\xi-\xi')} \frac{\mathrm{e}^{\xi'}}{(1+\mathrm{e}^{\xi'})^2}\,\mathrm{d}\xi'\right]. \tag{6.25}$$

Since f_v^1 is a symmetric function of ξ (equation (6.25)), it can be calculated for positive ξ by making the substitution $t = \mathrm{e}^{\xi'-\xi}$. After integrating by parts,

$$f_v^1 = \frac{u^2}{2}\left[\int_1^{\infty} \frac{t^{-u-1}}{1+z^{-1}t}\,\mathrm{d}t - \int_{-\infty}^{1} \frac{t^{u-1}}{1+z^{-1}t}\,\mathrm{d}t\right], \tag{6.26}$$

with $z = \mathrm{e}^{-\xi}$. There is an explicit solution in terms of Lerch functions $\Phi(-z, 1, \pm\hat{u})$ (Gradshteyn & Ryzhik 1994),

$$f_v^1(z, \hat{u}) = -\frac{\hat{u}^2}{2}\left[\Phi(-z, 1, \hat{u}) + \Phi(-z, 1, -\hat{u}) + \pi \csc(\pi\hat{u}) z^{\hat{u}}\right], \tag{6.27}$$

which is continuous (in $0 < z < 1$) for all $\hat{u}$; the last term cancels singularities in the Lerch functions when the third argument is a negative integer. The final integral for $\hat{\omega}^1$ was computed numerically (in Maple) over the domain $\xi > 0$, and agrees with figure 1 of Hinch & Bhatt (1990). The first-order growth rates, $\hat{\omega}^1$, for constant surface area and for the powder model are compared in figure 12. The decreasing surface area in the powder model reduces the strength of the instability relative to constant surface area, but the behaviour is qualitatively similar.

6.5. *Grain model:* $\hat{s} = (1-\hat{\phi})^{1/2}$

Intermediate between constant surface area and powder models are those which depend on some non-integer power of the solids volume fraction, $\hat{s} = (1-\hat{\phi})^{\eta}$. Here we consider the case $\eta = 1/2$, which has an explicit form for the base state (6.16). However, the solution of (6.2)–(6.4) is complicated by the derivative $\hat{s}_b' \propto (1-\hat{\phi})^{-1/2}$ in (6.3), which diverges at the front. To eliminate the diverging terms, we replace the porosity as an independent variable by the specific surface area, so the three fields are now $\hat{s}$, $\hat{c}$ and $\hat{v}_\xi$. Repeating the analysis of appendix A, but replacing $\hat{\phi}$ with $(1-s)^2$ in (2.30) and (2.32), we obtain the following equations for the perturbations (in the limit $H \to 0$):

$$\delta\hat{v}_\xi(\partial_\xi \hat{c}_b) + \partial_\xi \delta\hat{c} = -\hat{s}_b \delta\hat{c} - \hat{c}_b \delta\hat{s}, \tag{6.28}$$

$$2(\partial_\tau - \partial_\xi)\delta\hat{s} = -\delta\hat{c}, \tag{6.29}$$

$$\partial_\xi^2 \delta\hat{v}_\xi + \partial_\eta^2 \delta\hat{v}_\xi = -2\hat{W}_b \hat{s}_b\left[(\partial_\xi \hat{s}_b)(\partial_\xi \delta\hat{v}_\xi) + \partial_\eta^2 \delta\hat{s}\right]. \tag{6.30}$$

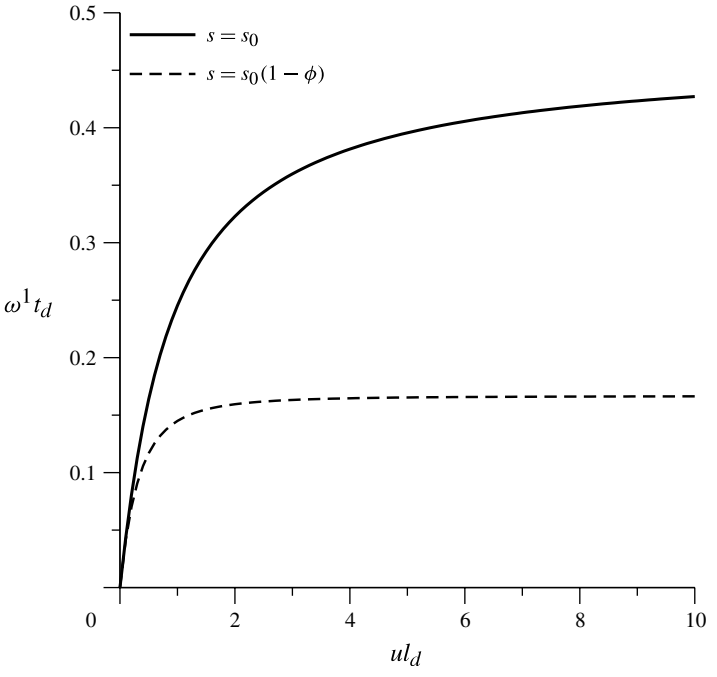

FIGURE 12. Dispersion curves in the limit of small permeability gradient, $\hat{W}_0 \to 0$. The first-order growth rates $\hat{\omega}^1(\hat{u})$ are shown for constant specific surface area (6.14) and for the powder model (6.15).

Expanding the perturbations as in (3.1)–(3.4), $\hat{s} = \hat{s}_b + f_s(\xi)\mathrm{e}^{\hat{\omega}\tau}\cos(\hat{u}\eta)$, and substituting the base solutions from (6.16):

$$\operatorname{sech}^2(\xi/2)\tanh(\xi/2)f_v = \left[2(\partial_\xi + \tanh(\xi/2))(\partial_\xi - \hat{\omega}) + \operatorname{sech}^2(\xi/2)\right]f_s, \tag{6.31}$$

$$2\tanh(\xi/2)\hat{W}_b\hat{u}^2 f_s = \left[\partial_\xi^2 + \operatorname{sech}^2(\xi/2)\tanh(\xi/2)\hat{W}_b\partial_\xi - \hat{u}^2\right]f_v, \tag{6.32}$$

where the concentration perturbation f_c has been eliminated in terms of f_s (equation (6.29)). The boundary condition $\hat{s}(\xi_f) = 0$ replaces (6.5) with

$$f_s(0) = \xi_0(-\partial_\xi \hat{s}_b)_0 = -\frac{\xi_0}{2}, \tag{6.33}$$

while the concentration boundary condition $f_c(\xi_f) = 0$ (equation (6.6)), with $(-\partial_\xi \hat{c}_b)_0 = 0$, can also be rewritten in terms of f_s,

$$(\partial_\xi f_s)_0 = \hat{\omega} f_s(0) = -\frac{\xi_0}{2}\hat{\omega}. \tag{6.34}$$

Equations (6.31) and (6.32) cannot in general be reduced to a single equation in either f_s or f_v, because each field is multiplied by $\tanh(\xi/2)$, which vanishes at the front. However, if the matrix is entirely soluble, for example the ISF model (6.10) or the Carman–Kozeny model (6.13), the permeability diverges as $\phi \to 1$. Then we can

eliminate f_s in favour of f_v, since the product $\tanh(\xi/2)\hat{W}_b$ is always positive;

$$\left[(\partial_\xi + t)(\partial_\xi - \hat{\omega}) + \frac{1-t^2}{2}\right]\left[(t\hat{W}_b)^{-1}(\partial_\xi^2 - \hat{u}^2) + (1-t^2)\partial_\xi\right] f_v = \hat{u}^2 t(1-t^2) f_v, \quad (6.35)$$

where $t = \tanh(\xi/2)$.

The downstream boundary conditions eliminate two solutions, rather than three as in the diffusive case; $f_v(\xi \to \infty) \sim A\mathrm{e}^{-\xi} + B\mathrm{e}^{-\hat{u}\xi}$. Two additional boundary conditions are needed at the front to solve for f_v and $\hat{\omega}$, or three if the amplitude of the perturbation is included explicitly. Equations (6.33) and (6.34) can be rewritten in terms of f_v using (6.32), which near the front becomes

$$2\hat{u}^2 f_s = \left[\frac{\xi}{2}(\partial_\xi^2 - \hat{u}^2) + \left(1 - \frac{\xi^2}{4}\right)\partial_\xi + \mathscr{O}(\xi^3)\right] f_v; \quad (6.36)$$

here we have made use of the fact that in the ISF (6.10) and CKG (6.13) models the permeability diverges as $(1-\hat{\phi})^{-1}$ so that $(tW_b)^{-1} \to \xi/2 + \mathscr{O}(\xi^3)$ as $\xi \to 0$. The two boundary conditions, (6.33) and (6.34), are then

$$(\partial_\xi f_v)_0 = 2\hat{u}^2 f_s(0) = -\xi_0 \hat{u}^2, \quad (6.37)$$

$$3(\partial_\xi^2 f_v)_0 - \hat{u}^2 f_v(0) = 4\hat{u}^2(\partial_\xi f_s)_0 = -2\xi_0 \hat{u}^2 \hat{\omega}. \quad (6.38)$$

Equation (6.37) is equivalent to the pressure boundary condition (6.9), which is not independent in this case. However there is an additional condition from the behaviour of (6.31) near the front,

$$\frac{\xi}{2} f_v = \left[(2\partial_\xi + \xi)(\partial_\xi - \hat{\omega}) + 1 + \mathscr{O}(\xi^2)\right] f_s; \quad (6.39)$$

for $f_v(0)$ to remain finite, it follows that $2(\partial_\xi^2 f_s)_0 - 2\hat{\omega}(\partial_\xi f_s)_0 + f_s(0) = 0$, which gives the final boundary condition

$$4(\partial_\xi^3 f_v)_0 - (1+2\hat{u}^2)(\partial_\xi f_v)_0 = 4\hat{u}^2(\partial_\xi^2 f_s)_0 = \xi_0 \hat{u}^2(1-2\hat{\omega}^2). \quad (6.40)$$

Equation (6.35), together with boundary conditions (6.37), (6.38) and (6.40), has been solved with the spectral method described in appendix C. It is convenient to rewrite the boundary conditions in an equivalent form:

$$3(\partial_\xi^2 f_v)_0 - 2\hat{\omega}(\partial_\xi f_v)_0 - \hat{u}^2 f_v(0) = 0, \quad 2(\partial_\xi^3 f_v)_0 - (\hat{u}^2 + \hat{\omega}^2)(\partial_\xi f_v)_0 = 0, \quad (6.41)$$

with $f_v(0) = 1$ as the (arbitrary) amplitude of the perturbation.

Dispersion curves are shown in figure 13 using the Carman–Kozeny permeability with different values of the porosity contrast $\Delta = (1-\phi_0)/\phi_0$ (equation (6.13)). In the limit $\Delta \to 0$ the permeability model reduces to the ISF model (6.10). Unlike the case of constant surface area, the growth rates for variable surface area asymptote to a constant value at large $\hat{u}$. When the porosity contrast is small the growth rate increases monotonically with $\hat{u}$, but for sufficiently large contrast $\Delta \sim 10$ there is once again a maximum in the growth rate; in this case the maximum is more pronounced than the data in figure 10.

7. Discussion

We begin the discussion by highlighting the most important findings from the theoretical analysis in §§ 2–6. First, the reactive-infiltration instability is controlled by two length scales: the upstream length $l_u = D_1^L/v_0$, a result of the interplay

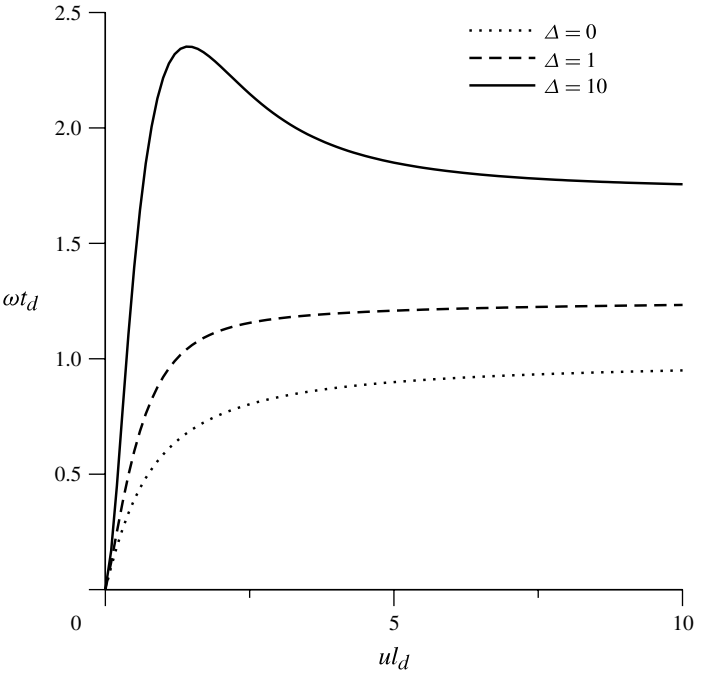

FIGURE 13. Dispersion curves for the grain model of the specific surface area, $\hat{s} = (1 - \hat{\phi})^{1/2}$. Growth rates for the Carman–Kozeny permeability relation (6.13) are shown in the convective ($H \to 0$) limit for various porosity contrasts: $\Delta = 0$ (dotted), which is equivalent to the ISF permeability (6.10), $\Delta = 1$ (dashed) and $\Delta = 10$ (solid).

between diffusive and convective transport, and the downstream length $l_d = 2D_0^L/(\sqrt{v_0^2 + 4D_0^L k s_0} - v_0)$ (equation (2.20)), where the reaction rate enters in as well. The profile of the reaction front (figure 2) is determined by the ratio of these lengths, l_d/l_u, which is a function of the dimensionless group $H = D_0^L k s_0 / v_0^2$ (equation (2.23)). The importance of this combination of parameters was recognized by Lichtner (1988) and Phillips (1990) in the context of reactive transport in rocks, while the relevance of the parameter H to wormhole growth was investigated by Steefel & Lasaga (1990). Nevertheless they did not incorporate their insights into a stability analysis, so the effects of H on the growth of the reactive-infiltration instability have only be recently recognized (Szymczak & Ladd 2013).

When $H = 0$, reactant transport is purely convective and l_u becomes negligible in comparison with l_d; the concentration field upstream of the front is then constant. Growth rates are positive at all wavelengths, and generally converge to a limit for asymptotically large u, as illustrated in figure 10. However, the shape of the dispersion curve depends strongly on the permeability gradient, the permeability–porosity relation, and the specific surface area model. Interestingly, if the permeability gradient is sufficiently high, a maximum appears in the dispersion curve (as observed in figures 10, 11 and 13), which implies wavelength selection even in the absence of diffusion; a similar phenomenon has been observed in fracture dissolution (Szymczak & Ladd 2011*a*) and in melt flow (Aharonov *et al.* 1995). For smaller gradients, the growth rate increases monotonically, with no wavelength selection.

If the permeability diverges at the maximum porosity, as in the ISF model (6.10) for example, the growth rate in the convective regime apparently increases without bound with increasing wavenumber (Sherwood 1987), as shown in figure 10(*a*). However, this result only occurs if the surface area is assumed to remain constant up until the point where all of the material is dissolved. A more realistic model, taking into account the reduction in reactive surface area (6.15) or (6.16), leads to an asymptotic growth rate at small wavelengths (figure 13).

The shape of the dispersion curve is much less dependent on permeability and reactive surface area when diffusive effects are taken into account. Diffusion always stabilizes the short wavelengths, which leads to a well-defined maximum growth rate. This is most clearly seen in the limit of small permeability gradient $\hat{W}_0 \ll 1$, where the dispersion relation can be obtained analytically; in terms of dimensional quantities the growth rate is (4.18)

$$\omega = \gamma_a \left[\frac{\hat{W}_0 v_0 u}{2(1 + u l_d)} - D^T u^2 \right] \tag{7.1}$$

independent of the particular form of the permeability relationship. An analysis of (7.1) leads to several important insights. First, the primary stabilizing factor is transverse dispersion, which acts to smooth out the concentration profile. In the small $\hat{W}_0$ limit, longitudinal dispersion plays no stabilizing role (§ 4.1.3); it only affects the penetration length of the base profile l_d. Second, any finite amount of (transverse) dispersion, $D^T > 0$, will result in a maximum in the growth rate and the eventual selection of a single length scale in the unstable front. Finally, for large enough u the growth rates are negative, which means that there is a lower limit to the lateral dimension of a system that can support an unstable dissolution front.

As H increases, diffusional stabilization reduces the growth rate and pushes the range of unstable wavelengths towards the origin, as can be seen in figures 3 and 4. For $H \geqslant 1$, the downstream kinetics plays a diminishing role, as l_d decreases in comparison with l_u. As $H \to \infty$ (with $\hat{W}_0 \ll 1$) the dispersion relation reaches the 'thin-front' limit $u l_d \to 0$,

$$\omega = \gamma_a \left[\frac{\hat{W}_0 v_0 u}{2} - D^T u^2 \right], \tag{7.2}$$

again independent of the permeability–porosity relation used. However, for large permeability contrast, equation (5.1) should be used (Chadam *et al.* 1986).

The general framework of the reactive-infiltration instability, presented in this paper, allows us to clarify the limits of applicability of earlier theories. Sherwood (1987) and Hinch & Bhatt (1990) considered a purely convective system (corresponding to $H = 0$ in our notation), and found the growth rate to be a monotonically increasing function of wavenumber. However, this is a singular limit, as shown in § 4.1.2; even a tiny diffusive contribution to the reactant flux stabilizes the small-scale perturbations and leads to a single dominant wavelength.

Chadam *et al.* (1986) and Ortoleva *et al.* (1987*a*) obtained a rather different dispersion relation (5.1) by neglecting the downstream penetration length. It is then simple to obtain the wavelengths corresponding to the maximum growth rate and the limiting system size that can sustain an unstable front (5.12). These results have been widely used to draw inferences about the mechanisms and growth rates for morphological changes in rocks, but the range of validity of these formula is

more restricted than is generally realized. Chadam *et al.* (1986) and Ortoleva *et al.* (1987*a*) claimed that the front-thickness can be ignored whenever the acid capacity is small ($\gamma_a \ll 1$), a condition that is widely applicable in nature. However, in these papers the reaction rate $k^\star$ was defined to include the solid concentration; in our notation $k^\star = k/c_{sol}$. Thus, the limit $\gamma_a \to 0$, while keeping $k^\star$ constant (Ortoleva *et al.* 1987*b*), implies that $k \to \infty$ (and hence $H \to \infty$) as well. Thus there is no general reduction of the reactive-infiltration instability to a Stefan-type problem, although it is appropriate in cases when H is sufficiently large. Confusion over the proper limiting process has persisted to the recent literature; for example, Zhao, Hobbs & Ord (2013) have extended the analysis of the thin-front limit to include finite acid capacity, without recognizing that the limit $H \to \infty$ has been imposed. Although Ortoleva *et al.* (1987*b*) have pointed out the thin-front limit requires a large reaction rate, they did not specify what k should be compared with; our analysis shows that the thin front limit is reached whenever $ks_0 \gg v_0^2/D^L$.

The reactive-infiltration instability is a wide-spread phenomenon that can occur in almost any system where reactive fluid flow results in a porosity increase. Importantly, it is not limited solely to dissolution but also to more complicated chemical alterations of rocks, which are very often accompanied by an increase in porosity increase (Pollok, Putnis & Putnis 2011). The models presented here allow for the estimate of the most important quantities characterizing the instability growth in these systems:

(i) the minimum width that allows for the development of an instability, λ_{min};
(ii) the maximally unstable wavelength, λ_{max};
(iii) the characteristic time of the instability development.

The above quantities are directly related to u_{lim} (the largest unstable wave vector) and u_{max} (the wave vector of the most unstable mode), plotted in figure 6.

To proceed further, we need estimates of the flow rates in porous rock. These depend on the formation, but are usually in the range $v_0 \approx 10^{-8}$–10^{-5} cm s^{-1} (Lake, Bryant & Araque-Martinez 2002). At these flow rates, dispersion can be assumed to be equal to the molecular diffusivity, $D \approx 10^{-5}$ cm^2 s^{-1}, which gives an upstream penetration length (l_u) in the range of 1 cm–10 m. If the reaction rate is sufficiently large that $H \gg 1$, the thin-front limit applies. Then, for a large permeability contrast $K_1 \gg K_0$, the maximally unstable wavelength $\lambda_{max} \sim 20 l_u$, or 10 cm–100 m. This constitutes a lower limit for the instability wavelength in diffusion-dominated dissolution.

Away from the thin-front limit the analysis is more complicated. Since the parameter characterizing the dissolution is the dimensionless group H (equation (2.23)), the wide range of reaction rates occurring in minerals makes it possible for convection-dominated or diffusion-dominated dissolution to take place at similar flow rates. For example, the formation of uranium roll fronts can be either convection-dominated or diffusion dominated (Szymczak & Ladd 2013), despite the small Péclet numbers typical of geophysical flows, because the reaction rate is small $ks_0 \sim 10^{-8}$ s^{-1}. On the other hand, acidization can be dispersion dominated (Szymczak & Ladd 2013) despite the much higher flow rates, because the reaction rates are large, with ks_0 up to 1 s^{-1}. Some estimates of scales of dissolution patterns ranging from millimetres to kilometres are given in Szymczak & Ladd (2013). One important conclusion from this analysis is that for a given rock–fluid system there is a minimum value of the most unstable wavelength λ_{max} as a function of fluid velocity. As the velocity increases the upstream length decreases, leading to smaller values of λ_{max}, but at the point where $H \sim 1$,

the downstream length takes over and the scale of the instability starts to increase (Szymczak & Ladd 2013).

In this paper we have analysed the stability of a steadily propagating dissolution front separating regions of high and low porosity. However, in some systems a uniform front may not have sufficient time to be formed before the instability develops. This 'initial' instability (Szymczak & Ladd 2011*a*), acting before the front is fully formed, has different characteristics from the 'moving front' instability investigated here; in many respects it resembles the instabilities in fractured rocks, described in Part I (Szymczak & Ladd 2012). The relative importance of the two mechanisms depends on porosity contrast, Δ, with the 'initial' instability developing in the formations where the proportion of easily soluble material is large, $\Delta \gg 1$.

Finally, we note that there are significant limitations to the use of a linear stability analysis to interpret geological morphologies. As the instability develops, competition between different fingers causes the shorter ones to be arrested (Szymczak & Ladd 2006), which can be seen in terra-rossa fingers (Szymczak & Ladd 2013) and also in maps of uraninite formations (Dahlkamp 2009). This nonlinear coupling leads to a coarsening of the pattern with an increasing average spacing between the fingers. The most unstable wavelength in the linear stability analysis thus sets a lower bound to wavelengths that might be expected in nature. Further work is needed to develop a quantitative understanding of the coarsening of the dissolution pattern.

Acknowledgements

This work was supported by the National Science Centre (Poland) under research Grant No. 2012/07/E/ST3/01734 and by the US Department of Energy, Chemical Sciences, Geosciences and Biosciences Division, Office of Basic Energy Sciences (DE-FG02-98ER14853). We would like to acknowledge the hospitality of the Isaac Newton Institute (Cambridge, UK) where some of the manuscript was prepared. Computations in this paper were performed by using Maple™13 and Mathematica™7.0.

Supplementary data

Supplementary data are available at http://dx.doi.org/10.1017/jfm.2013.586.

Appendix A. Linear stability analysis

Beginning with the coupled equations for flow, transport and reaction (2.29)–(2.32), we consider small perturbations about the base solutions for porosity, $\hat{\phi}_b$, velocity, $\hat{\boldsymbol{v}}_b$, and concentration, c_b:

$$\hat{\phi} = \hat{\phi}_b + \delta\hat{\phi}, \tag{A 1}$$

$$\hat{c} = \hat{c}_b + \delta\hat{c}, \tag{A 2}$$

$$\hat{v}_\xi = 1 + \delta\hat{v}_\xi, \tag{A 3}$$

$$\hat{v}_\eta = \delta\hat{v}_\eta. \tag{A 4}$$

The following linearized equations for the aperture, concentration and flow fields are obtained:

$$\delta\hat{v}_\xi(\partial_\xi\hat{c}_b) + \partial_\xi\delta\hat{c} - \hat{\boldsymbol{\nabla}}\cdot\hat{\boldsymbol{D}}_b\cdot\hat{\boldsymbol{\nabla}}\delta\hat{c} - \hat{\boldsymbol{\nabla}}\cdot\delta\hat{\boldsymbol{D}}\cdot\hat{\boldsymbol{\nabla}}\hat{c}_b = -(\partial_\tau - \partial_\xi)\delta\hat{\phi}, \tag{A 5}$$

$$(\partial_\tau - \partial_\xi)\delta\hat{\phi} = (1 + \hat{D}_0^L)(\hat{s}_b\delta\hat{c} + \delta\hat{s}\hat{c}_b), \tag{A 6}$$

$$\partial_\xi^2 \delta\hat{v}_\xi + \partial_\eta^2 \delta\hat{v}_\xi = \hat{W}_b \left[(\partial_\xi \hat{\phi}_b)(\partial_\xi \delta\hat{v}_\xi) + \partial_\eta^2 \delta\hat{\phi} \right], \tag{A 7}$$

where the incompressibility condition (2.31) was used to eliminate δv_η from the compatibility relation (A 7). The subscript b indicates the base state, $\hat{s}_b = \hat{s}(\hat{\phi}_b)$, $\hat{W}_b = \hat{W}(\hat{\phi}_b)$ and $\hat{\boldsymbol{D}}_b = \hat{\boldsymbol{D}}(\hat{\phi}_b, \hat{\boldsymbol{v}}_b = \boldsymbol{e}_\xi)$.

The variation in specific surface area can be projected onto the porosity field:

$$\delta\hat{s} = \hat{s}(\hat{\phi}_b + \delta\hat{\phi}) - \hat{s}(\hat{\phi}_b) = \hat{s}_b' \delta\hat{\phi}, \tag{A 8}$$

where the prime indicates a derivative with respect to porosity (3.11). Similarly, from the constitutive model for the diffusivity (2.4), $\hat{\boldsymbol{D}} = \hat{\boldsymbol{D}}_b + \delta\hat{\boldsymbol{D}}$ with

$$\hat{\boldsymbol{D}}_b = \begin{pmatrix} \hat{D}_b^L & 0 \\ 0 & \hat{D}_b^T \end{pmatrix}, \tag{A 9}$$

$$\delta\hat{\boldsymbol{D}} = \begin{pmatrix} (\hat{D}_b^L)' & 0 \\ 0 & (\hat{D}_b^T)' \end{pmatrix} \delta\hat{\phi} + \begin{pmatrix} (\hat{D}_b^L - \hat{D}_b^E)\delta\hat{v}_\xi & (\hat{D}_b^L - \hat{D}_b^T)\delta\hat{v}_\eta \\ (\hat{D}_b^L - \hat{D}_b^T)\delta\hat{v}_\eta & (\hat{D}_b^T - \hat{D}_b^E)\delta\hat{v}_\xi \end{pmatrix}, \tag{A 10}$$

where the prime again indicates a derivative with respect to porosity. The coefficients describing the dispersion in the base state have been replaced by differences in the base-state dispersion tensor itself $\Theta_b^{L,T} v_0 = D_b^{L,T} - D_b^E$.

Substituting the results from (A 9)–(A 10) into the transport equation (A 5),

$$\begin{aligned} &\delta\hat{v}_\xi(\partial_\xi \hat{c}_b) + \partial_\xi \delta\hat{c} - \partial_\xi \hat{D}_b^L \partial_\xi \delta\hat{c} - \hat{D}_b^T \partial_\eta^2 \delta\hat{c} - \partial_\xi(\hat{D}_b^L - \hat{D}_b^E)(\partial_\xi \hat{c}_b)\delta\hat{v}_\xi \\ &\quad - (\hat{D}_b^L - \hat{D}_b^T)(\partial_\xi \hat{c}_b)\partial_\eta \delta\hat{v}_\eta - \partial_\xi (\hat{D}_b^L)'(\partial_\xi \hat{c}_b)\delta\hat{\phi} = -(\partial_\tau - \partial_\xi)\delta\hat{\phi}. \end{aligned} \tag{A 11}$$

The corresponding equation for the upstream field, from (2.33), is

$$\begin{aligned} &\delta\hat{v}_\xi^u(\partial_\xi \hat{c}_b^u) + \partial_\xi \delta\hat{c}^u - \hat{D}_1^L \partial_\xi^2 \delta\hat{c}^u - \hat{D}_1^T \partial_\eta^2 \delta\hat{c}^u \\ &\quad - (\hat{D}_1^T - \hat{D}_1^E)(\partial_\xi \hat{c}_b^u)\partial_\xi \delta\hat{v}_\xi^u - (\hat{D}_1^L - \hat{D}_1^E)(\partial_\xi^2 \hat{c}_b^u)\delta\hat{v}_\xi^u = 0, \end{aligned} \tag{A 12}$$

where $\hat{\boldsymbol{D}}_1 = \hat{\boldsymbol{D}}_b(\hat{\phi} = 1)$ is the base-state dispersion tensor evaluated at the maximum porosity.

Substituting the perturbations from (3.1)–(3.3) into (A 11) leads to the first equation in (3.5). The operators $\mathscr{L}_{vv}$, $\mathscr{L}_{vc}$ and $\mathscr{L}_{v\phi}$ can be identified from the projections of (A 11) onto $\delta\hat{v}_\xi$, $\delta\hat{c}$ and $\delta\hat{\phi}$, respectively. Upstream of the front, the first equation in (3.12) follows from (A 12) in the same way. The remaining equations in (3.5) and (3.12) follow in similar fashion from (A 6), (A 7) and (2.34).

Appendix B. Small permeability gradient: $\hat{W}_0 \ll 1$

Expanding f_v, f_ϕ and $\hat{\omega}$ in powers of $\hat{W}_0$,

$$f_v = f_v^0 + \hat{W}_0 f_v^1 + \cdots, \quad f_\phi = f_\phi^0 + \hat{W}_0 f_\phi^1 + \cdots, \quad \hat{\omega} = \hat{\omega}^0 + \hat{W}_0 \hat{\omega}^1 + \cdots, \tag{B 1}$$

then at zeroth order, from (4.4), there is a homogeneous equation for the velocity perturbation, $(\partial_\xi^2 - \hat{u}^2) f_v^0 = 0$, with a decaying solution

$$f_v^0 = A_v \mathrm{e}^{-\hat{u}\xi}. \tag{B 2}$$

However, this solution can only satisfy the boundary condition at the front (4.8) when $A_v = 0$. Then, from (4.3), the equation for f_ϕ^0 is $\mathscr{L}_\phi^0 f_v^0 = 0$, where $\mathscr{L}_\phi^0$ indicates that $\hat{\omega}$

in (4.7) should be replaced by $\hat{\omega}^0$. It has a decaying solution

$$f_\phi^0 = A_\phi \mathrm{e}^{\lambda_\phi \xi}, \tag{B 3}$$

where λ_ϕ is the negative root of the characteristic equation for the operator $\mathscr{L}_\phi$ (equation (4.7)),

$$\lambda_\phi = \frac{1 - \sqrt{(1 + 2\hat{D}^L)^2 + 4\hat{D}^L\hat{D}^T\hat{u}^2}}{2\hat{D}^L}. \tag{B 4}$$

The final boundary condition (4.9) gives an equation for the zeroth-order growth rate

$$(\hat{\omega}^0 - \lambda_\phi)(\lambda_\phi - \lambda_c) = -\left(1 + \frac{1}{\hat{D}^L}\right), \tag{B 5}$$

with the solution given in (4.12),

$$\hat{\omega}^0 = \frac{1}{\hat{D}^L} - \lambda_c. \tag{B 6}$$

At first order (in $\hat{W}_0$) there are coupled inhomogeneous equations for f_v^1 and f_ϕ^1, from (4.3)–(4.4):

$$(\partial_\xi^2 - \hat{u}^2) f_v^1 = -A_\phi \hat{u}^2 \mathrm{e}^{\lambda_\phi \xi}, \tag{B 7}$$

$$\mathscr{L}_\phi^0 f_\phi^1 = -(1 + \hat{D}^L)\mathscr{L}_{vu} f_v^1. \tag{B 8}$$

Since f_ϕ^0 is in the kernel of $\mathscr{L}_\phi$ there are no other terms in (B 8). The decaying solution for f_v^1 satisfying the boundary condition (4.8),

$$f_v^1 = -A_\phi \left(\frac{\hat{u}}{2(\lambda_\phi + \hat{u})}\mathrm{e}^{-\hat{u}\xi} + \frac{\hat{u}^2}{\lambda_\phi^2 - \hat{u}^2}\mathrm{e}^{\lambda_\phi \xi}\right), \tag{B 9}$$

acts as a forcing term in (B 8), $f_\phi^1 = C_0 \mathrm{e}^{\lambda_\phi \xi} - (\mathscr{L}_\phi^0)^{-1}(1 + D^L)\mathscr{L}_{vu} f_v^1$;

$$f_\phi^1 = A_\phi \left(C_0 \mathrm{e}^{\lambda_\phi \xi} + C_1 \mathrm{e}^{-(\hat{u}+1)\xi} + C_2 \mathrm{e}^{(\lambda_\phi - 1)\xi}\right). \tag{B 10}$$

The coefficients C_1 and C_2 are

$$C_1 = \frac{1 + \hat{D}^L - \hat{D}^E + (\hat{D}^T - \hat{D}^E)\hat{u}}{2(\lambda_\phi + \hat{u})(\hat{\omega}^0 + \hat{u} + 1)\left[1 + 2\hat{D}^L + (\hat{D}^L - \hat{D}^T)\hat{u}\right]}, \tag{B 11}$$

$$C_2 = \frac{\left[1 + \hat{D}^L - \hat{D}^E - (\hat{D}^T - \hat{D}^E)\lambda_\phi\right]\hat{u}^2}{(\lambda_\phi^2 - \hat{u}^2)(\hat{\omega}^0 - \lambda_\phi + 1)\left[1 + \hat{D}^L(1 - 2\lambda_\phi)\right]}, \tag{B 12}$$

and $C_0 = -C_1 - C_2$ is chosen so that $f_\phi^1(0) = 0$.

The remaining boundary condition (4.9),

$$\left[\hat{\omega}^1(\partial_\xi - \lambda_c)f_\phi^0\right]_0 + \left[(\hat{\omega}^0 - \partial_\xi)(\partial_\xi - \lambda_c)f_\phi^1\right]_0 = (1 + D^L)\Lambda(0)\left(\lambda_c - \frac{1}{\hat{D}^L} - \hat{u}\right) f_v^1(0), \tag{B 13}$$

can be used to find the first-order contribution to the growth rate:

$$\hat{\omega}^1 = (\hat{\omega}^0 - \lambda_\phi)(C_1 + C_2) - \frac{(1+\hat{u}+\lambda_c)(1+\hat{u}+\hat{\omega}^0)}{\lambda_c - \lambda_\phi} C_1 - \frac{(1+\lambda_c-\lambda_\phi)(1+\hat{\omega}^0-\lambda_\phi)}{\lambda_c-\lambda_\phi} C_2 + \frac{\hat{u}(\hat{\omega}^0+\hat{u})(1+\hat{D}^L)\Lambda(0)}{2(\lambda_c-\lambda_\phi)(\hat{u}-\lambda_\phi)}, \tag{B 14}$$

where λ_c, λ_ϕ and $(1+\hat{D}^L)\Lambda(0)$ are given in (3.26), (B 4) and (4.10).

Appendix C. Spectral method

In general, numerical methods must be used to solve for the instability growth rate; in this paper results are limited to cases where the base solutions and their spatial derivatives can be found explicitly, which significantly simplifies the calculations. For constant specific surface area and dispersion (§ 4), the coupled differential equations in (3.5) can be converted to a single fifth-order equation for the velocity perturbation,

$$\left\{ \mathscr{L}_{vv} + \left[\mathscr{L}_{vc}(1+D_0^L)^{-1}\mathscr{L}_{c\phi} + \mathscr{L}_{v\phi} \right] (-\hat{W}_b\hat{u}^2)^{-1} \mathscr{L}_{\phi v} \right\} f_v = 0, \tag{C 1}$$

which was solved using a spectral method (Boyd 1987, 2001). The perturbation $f_v(\xi)$ is expanded in a finite Chebyshev basis,

$$f_v(\xi) = \sum_{j=1}^{N} g_j T_{j-1}\left(\frac{\xi - L}{\xi + L}\right), \tag{C 2}$$

which automatically eliminates solutions that diverge in the far field $\xi \to \infty$.

The asymptotic ($\xi \to \infty$) form of (C 1), $\mathscr{L}_\phi(\partial_\xi^2 - \hat{u}^2)f_v = 0$ (equation (4.7)), shows that there are only two decaying solutions in the far field, $\mathrm{e}^{\lambda_\phi \xi}$ and $\mathrm{e}^{-\hat{u}\xi}$, where λ_ϕ is the negative eigenvalue of $\mathscr{L}_\phi$ (equation (B 4)). The choice of decaying basis functions, imposed by the far-field boundary conditions in (3.16)–(3.18), automatically eliminates three solutions. Only two boundary conditions, (3.29) and (3.31), are then needed to close the downstream equations (taking the amplitude of the perturbation $\xi_0 = 1$). The remaining boundary condition (3.34) determines the growth rate $\hat{\omega}$ for a given $\hat{u}$. Starting with a pair of guesses for $\hat{\omega}$, the residuals from (3.34) are used to provide an improved value of $\hat{\omega}$ using the secant method. Typically 5–10 iterations are sufficient for convergence. We seek the largest eigenvalue that satisfies (3.34), corresponding to the maximum growth rate for that wavelength. Further details of the implementation can be found in § 5 of Szymczak & Ladd (2012).

The accuracy of the spectral method is dependent on the mapping parameter L in (C 2) and the number of basis functions. In most cases 4–5 figure accuracy was achieved with 40–80 basis functions, with L varying between 10 and 100 depending on the wavenumber. More basis functions are needed to maintain accuracy near the diffusive limit ($H \gg 1$); here convergence to within 1 % requires no more than 100–200 basis functions.

The equations were solved by a combination of analytic and numerical methods cross-checking independent calculations with both Maple™ and Mathematica™; example worksheets (Maple) are included in the supplementary material available at http://dx.doi.org/10.1017/jfm.2013.586. The worksheet *spectralH.mw* was used to generate the results in § 4.2; since dispersion can be neglected ($D^E = D^T = D^L$) it was

simpler to solve for f_ϕ rather than f_v:

$$\left[\mathscr{L}_{\phi v}\mathrm{e}^{\xi}\mathscr{L}_{vc}\mathscr{L}_{c\phi}+\hat{W}_b\hat{u}^2\right]f_\phi=0. \tag{C 3}$$

As before (Szymczak & Ladd 2012), we must solve for the related eigenfunction $g_\phi=\mathrm{e}^{\xi}f_\phi$, to ensure that the far-field boundary condition is applied to all the decaying solutions. Calculations in the convective limit, for varying permeability models but constant surface area (§ 6.3), were solved using *spectralC.mw*. Finally, the dispersion relation for the grain model (6.35) is solved in *spectralG.mw*.

Appendix D. Boundary conditions in the thin-front limit

In the thin-front limit ($H\to\infty$), all of the reactant is consumed in an infinitesimal region around the front and the downstream length scale (l_d) vanishes. On the scale of the upstream penetration length (l_u) the concentration exactly vanishes at the front. There is then no convective flux across the front and the dispersive reactant flux must balance the rate of consumption, $R_f(y,t)$,

$$R_f=-\boldsymbol{n}\cdot(\boldsymbol{D}\cdot\nabla c^u)_{x=x_f}, \tag{D 1}$$

where the normal to the front, $\boldsymbol{n}$, is pointing in the downstream direction. Linearizing the concentration field and dispersion tensor (A 9)–(A 10) about the upstream base state, the dispersive flux can be related to the front velocity,

$$\nu c_{sol}\Delta\frac{\mathrm{d}x_f}{\mathrm{d}t}=R_f=-\left[D_1^L\partial_{x'}c_b^u+D_1^L\partial_{x'}\delta c^u+(D_1^L-D_1^E)\delta v_{x'}^u\partial_{x'}c_b^u\right]_{x'=x_f'}; \tag{D 2}$$

other terms in the dispersive flux only contribute at second order and beyond.

The upstream length l_u is used to scale length and time:

$$\zeta=\frac{x'}{l_u},\quad \eta=\frac{y}{l_u},\quad \tau=\frac{v_0\gamma_a t}{l_u}. \tag{D 3}$$

We chose not to define new symbols for the dimensionless y coordinate (η) and time (τ) since they will only be used within this section; note that they are different from η and τ in the main text by a factor of l_d/l_u. The dimensionless form of (D 2) in the upstream scaling is

$$1+\frac{\mathrm{d}\zeta_f}{\mathrm{d}\tau}=-\left[\partial_\zeta\hat{c}_b^u+\partial_\zeta\delta\hat{c}^u+(1-\tilde{D}_1^E)\delta\hat{v}_\zeta^u\partial_\zeta\hat{c}_b^u\right]_{\zeta=\zeta_f}, \tag{D 4}$$

where $\tilde{D}_1^L=D_1^L/(v_0l_u)=1$ and $\tilde{D}_1^E=D_1^E/(v_0l_u)=D_1^E/D_1^L$.

In addition to the flux condition (D 4) we have continuity of the concentration itself,

$$\hat{c}_b^u(0)=0,\quad \hat{c}^u(\zeta_f)=0. \tag{D 5}$$

The base concentration from (3.22), $\hat{c}_b^u(\zeta)=1-\mathrm{e}^{\zeta}$, satisfies the boundary condition in (D 5) and balances the velocity of the steadily propagating front in (D 4). Expanding the concentration at ζ_f about $\zeta=0$ and taking the usual form for the front perturbation (3.24), $\zeta_f=\zeta_0\cos(\tilde{u}\eta)\mathrm{e}^{\tilde{\omega}\tau}$, we obtain two boundary conditions for the upstream concentration perturbation, f_c^u:

$$f_c^u(0)=\xi_0, \tag{D 6}$$

$$(\partial_\zeta f_c^u)_0=\xi_0(1-\tilde{\omega})+(1-\tilde{D}_1^E)f_v^u(0). \tag{D 7}$$

The base pressure in the upstream region is linear,

$$\hat{p}_b^u = \hat{p}_0 + \frac{\zeta}{\hat{K}_1}, \tag{D 8}$$

where $\hat{K}_1 = \hat{K}(\hat{\phi} = 1)$ is the maximum permeability and the dimensionless pressure $\hat{p}$ is defined as

$$\hat{p} = \frac{p}{(\partial_\zeta p_b)_{\zeta\to\infty}}. \tag{D 9}$$

With this scaling the velocity field is simply $\hat{\boldsymbol{v}} = \hat{K}\tilde{\boldsymbol{\nabla}}\hat{p}$. The pressure perturbation satisfies the Laplace equation (since $\hat{\phi} = 1$), and growing perturbations can be written as in (3.1),

$$\hat{p}^u = \hat{p}_b^u + \delta\hat{p}^u, \quad \delta\hat{p}^u = A_p \mathrm{e}^{\tilde{u}\zeta}\cos(\tilde{u}\eta)\mathrm{e}^{\tilde{\omega}\tau}, \tag{D 10}$$

where A_p is a constant to be determined.

The matching condition on the normal velocity is simply

$$f_v(0) = \hat{K}_1 A_p \tilde{u}, \tag{D 11}$$

but the pressure-matching condition is more complicated since the base pressure at the front is varying. After linearizing the upstream and downstream pressures about the base state, as in (3.28), the boundary condition for the downstream pressure is

$$f_p(0) - A_p = -\xi_0\left(\frac{1}{\hat{K}_0} - \frac{1}{\hat{K}_1}\right). \tag{D 12}$$

where $\hat{K}_0 = 1$ is the permeability on the downstream side of the front, $\xi = 0_+$.

The pressure perturbation f_p can be replaced by the velocity perturbation through the linearized constitutive equation $\delta\hat{v}_\eta = \hat{K}_b\partial_\eta\delta\hat{p}$ and the incompressibility condition (2.31)

$$\partial_\zeta f_v = \hat{K}_0\tilde{u}^2 f_p. \tag{D 13}$$

From (D 11) we can eliminate A_p in favour of f_v,

$$\hat{K}_1(\partial_\zeta f_v)_0 - \tilde{u}\hat{K}_0 f_v(0) = -\xi_0\tilde{u}^2(\hat{K}_1 - \hat{K}_0). \tag{D 14}$$

When the porosity is continuous across the front, the right-hand side vanishes and we obtain the simpler condition (3.31), but in the thin-front limit, the tangential velocities do not match. Taking the decaying solution at large ζ implies that $\partial_\zeta f_v = -\tilde{u}f_v$, and the boundary condition is then

$$f_v(0) = \xi_0\tilde{u}\left(\frac{\hat{K}_1 - \hat{K}_0}{\hat{K}_1 + \hat{K}_0}\right). \tag{D 15}$$

Appendix E. Asymptotic expansion at small wavelengths

At small wavelengths (large $\hat{u}$) the velocity perturbation is slaved to the porosity field (6.4), $f_v = \hat{W}_b f_\phi$, which can be found from the second-order equation

$$\left[\partial_\xi^2 + (1-\hat{\omega})\partial_\xi + \hat{W}_b\mathrm{e}^{-\xi} - \hat{\omega}\right] f_\phi = 0. \tag{E 1}$$

In the far field there is only one decaying solution, $f_\phi \sim \mathrm{e}^{-\xi}$, and therefore the boundary conditions on f_ϕ (equation (6.5)) and f_c (equation (6.6)) reduce to a condition on the eigenvalue, $\hat{\omega}$,

$$(\partial_\xi f_\phi)_0 = (\hat{\omega} - 1) f_\phi(0). \tag{E 2}$$

For constant $W_b = \hat{W}_0$, the decaying solution is $f_\phi \propto J_{\hat{\omega}+1}(2\hat{W}_0^{1/2}\mathrm{e}^{-\xi/2})$, which gives the asymptotic ($\hat{u} \to \infty$) growth rate as the largest root of the equation

$$J_{\hat{\omega}+1}(2\hat{W}_0^{1/2}) = \hat{W}_0^{1/2} J_{\hat{\omega}}(2\hat{W}_0^{1/2}). \tag{E 3}$$

Spectral solutions at large $\hat{u}$, with the permeability model from (6.11), agree with numerical solutions of (E 3).

REFERENCES

AHARONOV, E., WHITEHEAD, J., KELEMEN, P. & SPIEGELMAN, M. 1995 Channeling instability of upwelling melt in the mantle. *J. Geophys. Res.* **100**, 433–455.

BEAR, J. 1961 On the tensor form of dispersion in porous media. *J. Geophys. Res.* **66**, 1185–1197.

BOYD, J. P. 1987 Orthogonal rational functions on a semi-infinite interval. *J. Comput. Phys.* **70**, 63–88.

BOYD, J. P. 2001 *Chebyshev and Fourier Spectral Methods*. Dover.

CHADAM, D., HOFF, D., MERINO, E., ORTOLEVA, P. & SEN, A. 1986 Reactive infiltration instabilities. *J. Appl. Maths* **36**, 207–221.

CHADAM, J., ORTOLEVA, P., QIN, Y. & STAMICAR, R. 2001 The effect of hydrodynamic dispersion on reactive flows in porous media. *Euro. J. Appl. Maths* **12**, 557–569.

DACCORD, G. & LENORMAND, R. 1987 Fractal patterns from chemical dissolution. *Nature* **325**, 41–43.

DAHLKAMP, F. J. 2009 *Uranium Deposits of the World*. Springer.

DAINES, M. J. & KOHLSTEDT, D. L. 1994 The transition from porous to channelized flow due to melt/rock reaction during melt migration. *Geophys. Res. Lett.* **21**, 145–148.

DE WIT, A., ECKERT, K. & KALLIADASIS, S. 2012 Introduction to the focus issue: chemo-hydrodynamic patterns and instabilities. *Chaos* **22**, 037101.

DE WIT, A. & HOMSY, G. M. 1999 Viscous fingering in reaction–diffusion systems. *J. Chem. Phys.* **110**, 8663–8675.

FOGLER, H. S. & MCCUNE, C. C. 1976 On the extension of the model of matrix acid stimulation to different sandstones. *AIChE J.* **22**, 799–805.

GOLFIER, F., ZARCONE, C., BAZIN, B., LENORMAND, R., LASSEUX, D. & QUINTARD, M. 2002 On the ability of a Darcy-scale model to capture wormhole formation during the dissolution of a porous medium. *J. Fluid Mech.* **457**, 213–254.

GRADSHTEYN, I. S. & RYZHIK, I. M. 1994 *Tables of Integrals, Series, and Products*, 5th edn. Academic.

GROVES, C. G. & HOWARD, A. D. 1994 Early development of karst systems. I. Preferential flow path enlargement under laminar flow. *Water Resour. Res.* **30**, 2837–2846.

HINCH, E. J. & BHATT, B. S. 1990 Stability of an acid front moving through porous rock. *J. Fluid Mech.* **212**, 279–288.

HOMSY, G. M. 1987 Viscous fingering in porous media. *Annu. Rev. Fluid Mech.* **19**, 271–311.

KELEMEN, P., WHITEHEAD, J., AHARONOV, E. & JORDAHL, K. 1995 Experiments on flow focusing in soluble porous media, with applications to melt extraction from the mantle. *J. Geophys. Res.* **100**, 475–496.

LAKE, L., BRYANT, S. & ARAQUE-MARTINEZ, A. 2002 *Geochemistry and Fluid Flow*. Elsevier.

LICHTNER, P. C. 1988 The quasi-stationary state approximation to coupled mass transport and fluid-rock interaction in a porous media. *Geochim. Cosmochim. Acta* **52**, 143–165.

NOIRIEL, C., GOUZE, P. & BERNARD, D. 2004 Investigation of porosity and permeability effects from microstructure changes during limestone dissolution. *Geophys. Res. Lett.* **31**, L24603.

NOIRIEL, C., LUQUOT, L., MADÉ, B., RAIMBAULT, L., GOUZE, P. & VAN DER LEE, J. 2009 Changes in reactive surface area during limestone dissolution: an experimental and modelling study. *Chem. Geol.* **265**, 160–170.

ORTOLEVA, P. J. 1994 *Geochemical Self-organization*. Oxford University Press.

ORTOLEVA, P., CHADAM, J., MERINO, E. & SEN, A. 1987*a* Geochemical self-organization II: the reactive-infiltration instability. *Am. J. Sci.* **287**, 1008–1040.

ORTOLEVA, P., MERINO, E., MOORE, C. & CHADAM, J. 1987*b* Geochemical self-organization I. Reaction-transport feedbacks and modelling approach. *Am. J. Sci.* **287**, 979–1007.

PHILLIPS, O. M. 1990 Flow-controlled reactions in rock fabrics. *J. Fluid Mech.* **212**, 263–278.

POLLOK, K., PUTNIS, C. V. & PUTNIS, A. 2011 Mineral replacement reactions in solid solution-aqueous solution systems: volume changes, reactions paths and end-points using the example of model salt systems. *Am. J. Sci.* **311**, 211–236.

ROWAN, G. 1959 Theory of acid treatment of limestone formations. *J. Inst. Pet.* **45**, 321–334.

SHERWOOD, J. D. 1987 Stability of a plane reaction front in a porous medium. *Chem. Engng Sci.* **42**, 1823–1829.

SPIEGELMAN, M., KELEMEN, P. & AHARONOV, E. 2001 Causes and consequences of flow organization during melt transport: the reaction infiltration instability in compactable media. *J. Geophys. Res.* **106**, 2061–2077.

STEEFEL, C. I. & LASAGA, A. C. 1990 Evolution of dissolution patterns. In *Chemical Modelling of Aqueous Systems II* (ed. D. C. Melchior & R. L. Bassett), pp. 212–225. American Chemical Society.

SZYMCZAK, P. & LADD, A. J. C. 2006 A network model of channel competition in fracture dissolution. *Geophys. Res. Lett.* **33**, L05401.

SZYMCZAK, P. & LADD, A. J. C. 2011*a* The initial stages of cave formation: beyond the one-dimensional paradigm. *Earth Planet. Sci. Lett.* **301**, 424–432.

SZYMCZAK, P. & LADD, A. J. C. 2011*b* Instabilities in the dissolution of a porous matrix. *Geophys. Res. Lett.* **38**, L07403.

SZYMCZAK, P. & LADD, A. J. C. 2012 Reactive infiltration instabilities in rocks. Fracture dissolution. *J. Fluid Mech.* **702**, 239–264.

SZYMCZAK, P. & LADD, A. J. C. 2013 Interacting length scales in the reactive-infiltration instability. *Geophys. Res. Lett.* **40**, 3036–3041.

WANGEN, M. 2013 Stability of reaction-fronts in porous media. *Appl. Math. Model.* **37**, 4860–4873.

ZHAO, C., HOBBS, B. E. & ORD, A. 2013 Theoretical analyses of acidization dissolution front instability in fluid-saturated carbonate rocks. *Intl J. Numer. Anal. Meth. Geomech.* **37**, 2084–2105.